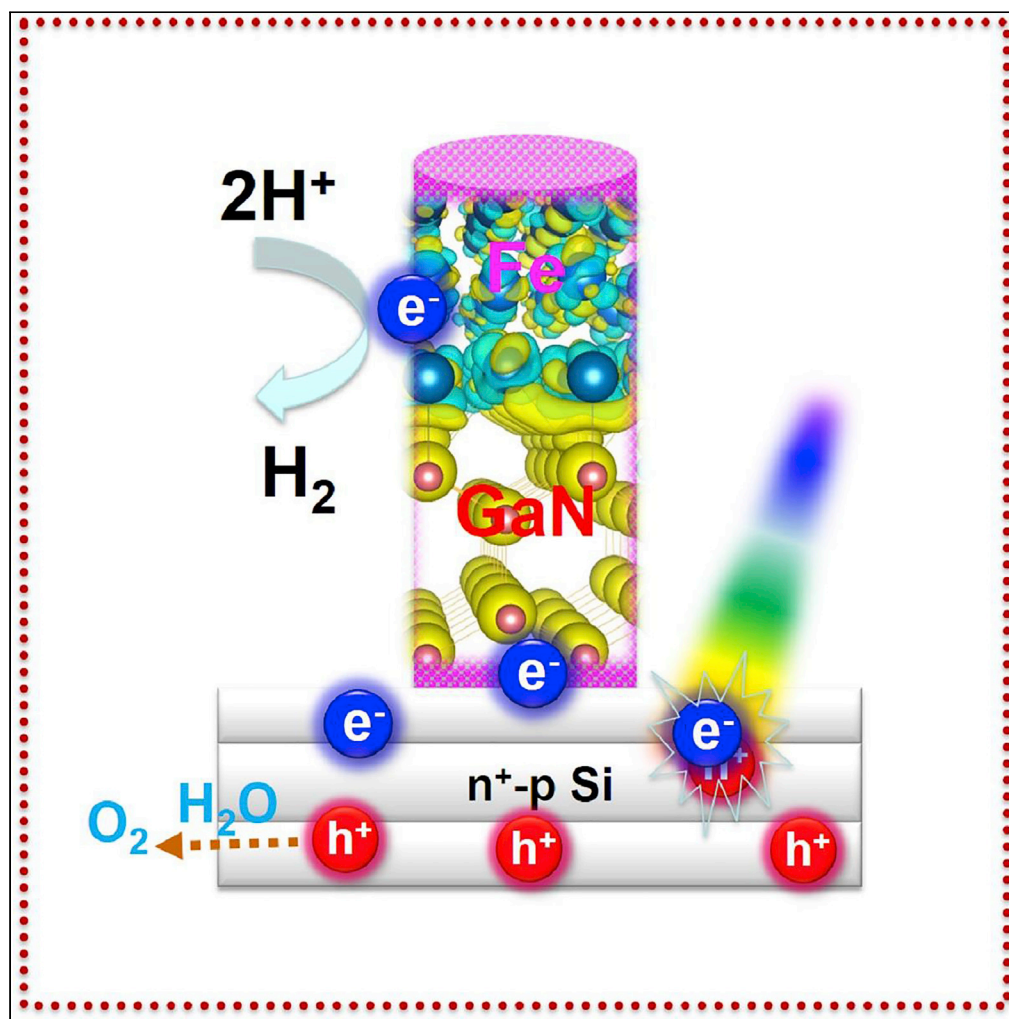Article

Few-Atomic-Layers Iron for Hydrogen Evolution from Water by Photoelectrocatalysis

Baowen Zhou, Pengfei Ou, Roksana Tonny Rashid, ..., Haiding Sun, Jun Song, Zetian Mi

jun.song2@mcgill.ca (J.S.)
ztmi@umich.edu (Z.M.)

HIGHLIGHTS

Few-atomic-layers iron was anchored on GaN nanowires as an efficient HER catalyst

The spatial-confinement and N-rich GaN is essential for forming atomic iron layers

Low hydrogen absorption free energy is theoretically revealed over Fe_{3L}:GaN

The device exhibits a prominent performance for PEC water splitting to H_2

CellPress
OPEN ACCESS

Article

Few-Atomic-Layers Iron for Hydrogen Evolution from Water by Photoelectrocatalysis

Baowen Zhou,[1,2,7] Pengfei Ou,[3,7] Roksana Tonny Rashid,[2,7] Srinivas Vanka,[1] Kai Sun,[4] Lin Yao,[5] Haiding Sun,[6] Jun Song,[3,*] and Zetian Mi[1,2,8,*]

SUMMARY

The carbon-free production of hydrogen from water splitting holds grand promise for the critical energy and environmental challenges. Herein, few-atomic-layers iron (Fe$_{FAL}$) anchored on GaN nanowire arrays (NWs) is demonstrated as a highly active hydrogen evolution reaction catalyst, attributing to the spatial confinement and the nitrogen-terminated surface of GaN NWs. Based on density functional theory calculations, the hydrogen adsorption on Fe$_{FAL}$:GaN NWs is found to exhibit a significantly low free energy of −0.13 eV, indicative of high activity. Meanwhile, its outstanding optoelectronic properties are realized by the strong electronic coupling between atomic iron layers and GaN(10$\bar{1}$0) together with the nearly defect-free GaN NWs. As a result, Fe$_{FAL}$:GaN NWs/n$^+$-p Si exhibits a prominent current density of $\sim$ −30 mA cm^{-2} at an overpotential of $\sim$0.2 V versus reversible hydrogen electrode with a decent onset potential of +0.35 V and 98% Faradaic efficiency in 0.5 mol/L KHCO$_3$ aqueous solution under standard one-sun illumination.

INTRODUCTION

Photoelectrocatalytic (PEC) water splitting by utilization of solar energy and electricity presents one carbon-free route for the production of hydrogen, which holds grand promise for the worldwide challenges that we face today (e.g., energy shortage, global warming, and environmental issues) (Vijselaar et al., 2018). An efficient HER catalyst is at the core of a PEC cell for solar-driven water splitting. Up to now, platinum is well known as the state-of-the-art HER electrocatalyst (Cheng et al., 2016). Unfortunately, the high price and low abundance severely limit its large-scale applications. In this context, the pursuit of noble-metal-free HER electrocatalysts has attracted considerable interest over the past decades (Hui et al., 2018; Ye et al., 2018; Gao et al., 2017; Arif et al., 2018). So far, a wide variety of earth-abundant materials such as phosphides (Wexler et al., 2018; Shi et al., 2016), and chalcogenides (Feng et al., 2018; Zhou et al., 2018; Meng et al., 2015) have been developed as promising substitutes for platinum arising from their low cost and high activity. However, their overall efficiencies are still far below the demand of commercial applications and acidic media is generally a prerequisite for these materials to produce hydrogen with high efficiency (Ji et al., 2015; Zhang et al., 2016). From the viewpoint of environmental accountability and sustainability, hydrogen evolution in near-neutral/alkaline medium is relatively benign compared with that conducted in strong acid aqueous solution (Zhao et al., 2018; Jin et al., 2014; Hashemi et al., 2015). It is therefore necessary to develop a new, efficient, and inexpensive electrocatalyst for PEC water splitting, especially in near-neutral/alkaline aqueous medium.

[FeFe]-hydrogenase, as one homogeneous metalloenzyme from green plant, is the most efficient HER biocatalyst, owing to its unique atomic structure, well-defined catalytic centers, and superior metal-utilization efficiency (Camara and Rauchfuss, 2012; Wodrich and Hu, 2018; Tard and Pickett, 2009; Pullen, et al., 2013; Le Goff et al., 2009). Inspired by this masterpiece of nature, tremendous efforts have been devoted to exploring iron-based hydrogenase mimics for water splitting toward hydrogen. For example, Klumer and co-workers reported an assembly of chromophores to a bis(thiolate)-bridged diiron ([2Fe$_2$S]) as catalyst for hydrogen production by using a modular supramolecular approach (Kluwer et al., 2009). Wu et al. developed a set of water-soluble [FeFe]-hydrogenase mimics and, by integrating with CdSe quantum dots, demonstrated superior activity for photocatalytic hydrogen production in water (Wang et al., 2013; Li et al.,

Figure 1. Schematic Diagram for the Decoration of Few-Atomic-Layers Iron onto N-Terminated GaN NWs by a Combination of Plasma-Assisted Molecular Beam Epitaxy with Electrodeposition

2013). In spite of significant progress, these homogeneous hydrogenase mimics are restricted by a series of shortcomings, including complex fabrication, inherent fragility, and great difficulty in scaling up to industrial applications.

Atomically dispersed metals are emerging as a rising star of heterogeneous catalysts with impressive homogeneous features such as well-defined catalytic centers, low-coordination environment, and high-efficiency atom utilization (Wang et al., 2018). In addition, atomic-level catalysts possess strong metal-support interactions and high surface energy, thus presenting great promise to achieve high performance for various chemical reactions. It is worth mentioning that atomically dispersed metals have grand potential in water splitting (Xue et al., 2018; Hui et al., 2019; Yu et al., 2019; Zhang et al., 2018). For example, atomic-scale cobalt was supported on nitrogen-doped graphene as an efficient and inexpensive electrocatalyst for hydrogen generation from water splitting, wherein catalytical sites are associated with the metal centers coordinated to nitrogen (Fei et al., 2015). Similarly, tuned by electrochemical methods, atomically dispersed nickel species were anchored on graphitized carbon for electrocatalytic water splitting toward hydrogen (Fan, et al., 2016). Despite great promise, the area of atomically dispersed metals in catalyzing hydrogen evolution reaction is still in the infant stage, and the exploration of heterogeneous atomic-level iron catalyst for hydrogen formation is of significance but particular challenge (Cao et al., 2017).

In this work, by utilizing the unique spatial confinement and N-terminated feature of GaN nanowire arrays (NWs), few-atomic-layers iron (Fe_{FAL}) is anchored onto the lateral surface of GaN NWs on wafer-scale n^+-p silicon junction as an efficient catalyst for PEC water splitting toward hydrogen. Theoretically, density functional theory (DFT) calculations suggest that few-atomic-layers iron is remarkably favorable for hydrogen evolution with an extremely low free energy of hydrogen adsorption. Moreover, strong electronic coupling between few-atomic-layers iron and GaN(10$\bar{1}$0) together with the well-defined GaN NWs with nearly defect-free structure enables superior optoelectronic properties. Experimentally, the monolithically integrated Fe_{FAL}:GaN NWs/n^+-p Si demonstrates high activity for water splitting toward hydrogen. A high photocurrent density of -15.6 mA cm^{-2} is acquired at 0 V versus RHE with a decent onset potential of +0.35 V and high Faradaic efficiency of 98% in 0.5 M KHCO$_3$ aqueous solution at argon atmosphere under standard one-sun illumination (AM 1.5 G, 100 mW cm^{-2}). It is worth noting that a nearly saturated and high current density of ~ -30 mA cm^{-2} is achieved at a minor overpotential of $\sim$0.2 V. To our best knowledge, this is the utilization of atom-scale iron as an inexpensive and efficient catalyst for hydrogen production in near-neutral/alkaline aqueous medium for the first time.

RESULTS AND DISCUSSION

Fabrication and Characterization of the Photocathodes

Vertically aligned GaN NWs were grown on 2-inch n^+-p silicon wafer (GaN NWs/n^+-p Si) by radio frequency plasma-assisted molecular beam epitaxy (PA-MBE) (please see Figures 1 and S1, and Transparent Methods section). By tailoring the growth conditions, e.g., growing under N-rich conditions, the epitaxial GaN NW surfaces were engineered to be terminated with abundant nitrogen atoms, not only for their top c-plane but also for the lateral nonpolar (10$\bar{1}$0) surfaces (Kibria et al., 2016). Such abundant nitrogen coordinating sites provide sufficient anchors for stabilizing atomically dispersed metals (Zhang et al., 2017; Li et al.,
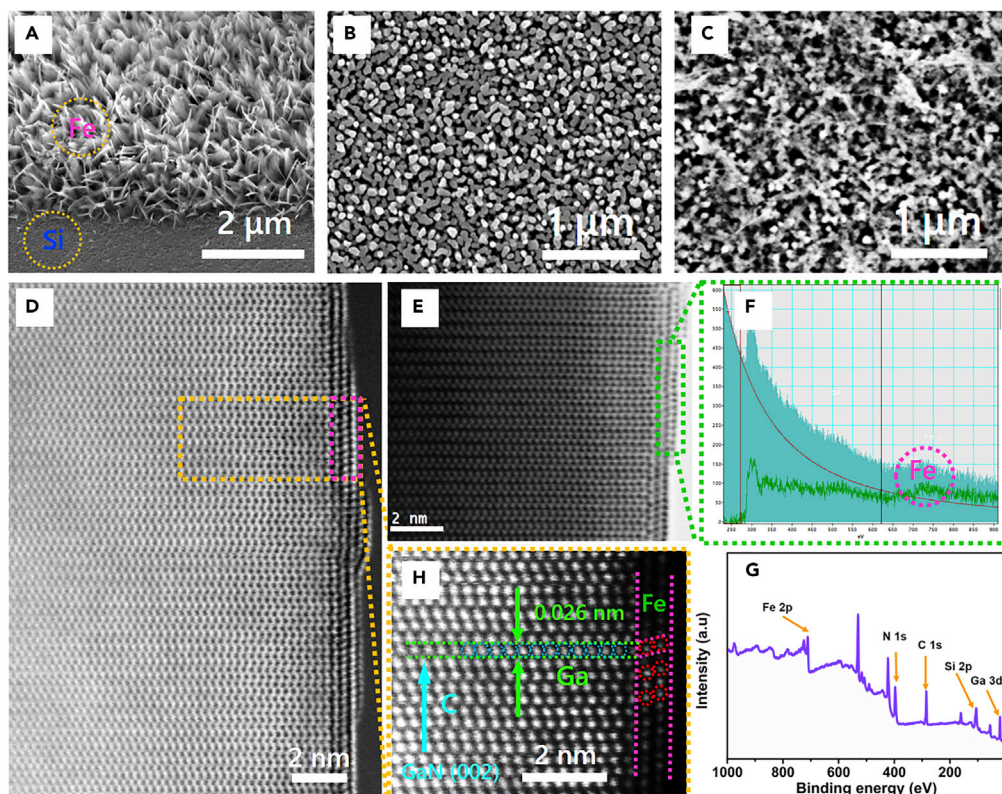
Figure 2. Structure and Composition Characterization

SEM images of Fe/n+-p Si (A), GaN NWs/n+-p Si (B), and Fe_FAL:GaN NWs/n+-p Si (C). STEM-LAADF, STEM-BF, and STEM-HAADF images of GaN NWs decorated with few-atomic-layers iron (D, E, and H), respectively. Extracted summed spectrum of few-atomic-layers iron decorated GaN NWs (F). XPS survey spectrum of Fe_FAL:GaN NWs/n+-p Si (G).

2018). What is more, the spatial confinement arising from nanowire arrays is favorable for atomically dispersed iron (Chen et al., 2018). As such, few-atomic-layers iron was readily deposited onto the lateral m-plane of GaN NWs by a simple electrocatalytic process (Figure 1). The morphology of Fe_x:GaN NWs/n+-p could be tailored by modulating the electrodeposition cycles (x denotes the number of deposition cycles). In the absence of GaN NWs, the iron cocatalyst was directly loaded on silicon through the identical process for comparison.

The structure and composition were characterized using scanning electron microscopy (SEM), scanning transmission electron microscopy (STEM), and X-ray photoelectron spectroscopy (XPS). The results are illustrated in Figure 2. SEM images in Figures 2A and S2 show that, in the absence of GaN NWs, the iron cocatalyst on silicon substrate (Fe/n+-p Si) exhibits a nanosheet-like morphology at hundred-nanometers level owing to the lack of nitrogen coordinating sites and spatial confinement. By the utilization of molecular beam epitaxy, N-terminated GaN NWs was epitaxially introduced onto silicon substrate with an average length of ~300 nm and diameter of ca. 50 nm (Figure S3). Moreover, as shown in the top-view SEM of GaN/n+-p Si in Figure 2B, the epitaxial GaN nanowire arrays are vertically aligned on silicon with relatively uniform spatial confinement. Such spatial confinement is essential for dispersing cocatalysts onto the lateral plane of GaN at atomic level. Using these nanowires as scaffolds, the iron cocatalyst could be loaded by electrodeposition, which does not significantly alter the nanowire arrays (Figure 2C). The low-angle annular dark-field scanning transmission electron microscopy (STEM-LAADF) image shows that the lateral surface of GaN nanowire is covered by few-atomic-layers iron with an intimate core/shell structure as highlighted in Figure 2D. The core with brighter intensity is attributed to be Ga atoms, whereas the dark layer is likely to be iron atoms since the image provides Z-contrast, wherein Z is the efficient atomic number. The bright-field scanning transmission electron microscopy (STEM-BF) image (Figure 2E) and corresponding composition extracted summed spectrum further verifies that the outer layers actually consisted of iron species (Figures 2F). High-resolution STEM images acquired from different models also corroborate the
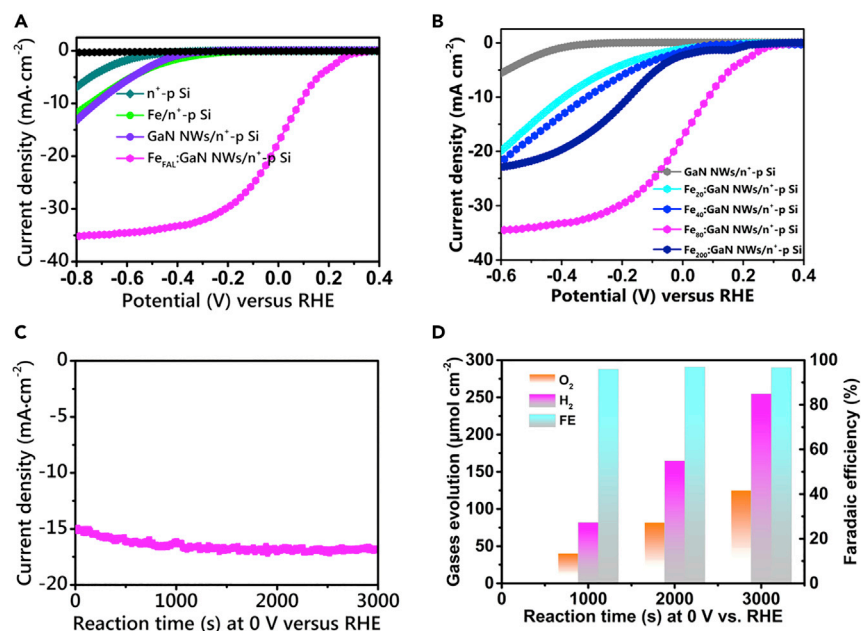
Figure 3. Photoelectrochemical Activity

(A) *J-V* curves of n^+-p Si, Fe/n^+-p Si, GaN NWs/n^+-p Si, and Fe_{FAL}:GaN NWs/n^+-p Si with 80 cycles of iron electrodeposition in argon-purged 0.5 M $KHCO_3$ aqueous solution under standard one-sun illumination. The black line is the *J-V* curve of Fe_{FAL}:GaN NWs/n^+-p Si under the identical conditions without illumination.

(B) Influence of the electro-depositing cycles of the iron catalyst on the performance.

(C) Current density of Fe_{FAL}:GaN NWs/n^+-p Si at 0 V versus RHE.

(D) The productivity of hydrogen and oxygen and Faradaic efficiency of Fe_{FAL}:GaN NWs/n^+-p Si for hydrogen evolution reaction. Experimental conditions: 0.5 M $KHCO_3$ aqueous solution, argon atmosphere, AM 1.5 G 100 mW cm^{-2}.

atomically dispersed iron on the lateral surface of GaN NWs (Figures S4 and S5). However, on the top of GaN NWs, despite of N-rich surface, Fe cocatalysts easily formed nanoclusters, owing to the lack of spatial confinements (Figure S6). Based on these characterizations, it is reasonable to conclude that both nitrogen-rich surface and spatial confinement of GaN NWs are indispensable for the formation of iron atomic layer (Chen et al., 2018). Herein, the morphological information is acquired from the as-synthesized sample with 80 cycles of iron electrodeposition (Fe_{80}:GaN NWs/n^+-p Si). Hereafter, the as-synthesized electrode at 80 cycles of iron electrodeposition is denoted as Fe_{FAL}:GaN NWs/n^+-p Si unless specially points out. XPS measurement confirmed that the iron species were successfully decorated on GaN/n^+-p Si (Figure 2G). Iron was found to exist in oxidized states, which was presumably due to the unavoidable oxidation for iron in water and air, particularly for those at nanoscale (Figure S7). X-ray diffraction spectroscopy characterization reveals the appearance of the feature peak of Fe_2O_3 (hematite) at 2-theta of 33.2° (JCPDS Data: PDF-33-0664) after the electrodeposition, whereas the featured peaks of GaN (002) at 2-theta of 34.5° remain intact (Figure S8). The successful decoration of iron catalysts does not only offer electron sinks for effectively extracting photoinduced electrons, but also provide active sites for catalyzing hydrogen evolution reaction, which is critical for high-efficiency HER. In addition, high-resolution STEM-HADDF image in Figure 2H shows that the inter-planar lattice spacing of GaN (002) is 0.26 nm, suggesting the c-axis growth direction of the nanowire. The GaN core is nearly defect-free and could favor efficient charge carrier transport. It has been well studied by our previous work and will be further discussed in the following section. What is more, the well-defined GaN NWs could maximize the catalytic iron centers, further enhancing the performance (Deng et al., 2019).

The Evaluation of PEC Water Splitting Performance

The PEC water splitting performance of Fe_{FAL}:GaN NWs/n^+-p Si as well as other working electrodes was tested using a three-electrode-configuration chamber (Figure S9). The working electrode was immersed in argon-purged 0.5 M $KHCO_3$ aqueous solution, and solar simulator was used as the light source (AM 1.5 G, 100 mW cm^{-2}). Both Pt counter electrode and Ag/AgCl reference electrode were separated from the working electrode by Nafion membranes to exclude the possibility that Pt was redeposited onto the

working electrode. As illustrated in Figure 3A, the onset potential of bare n^+-p silicon is negatively as low as −0.4 V with a low current density of −6 mA cm^{-2} at −0.8 V. The inferior performance could be attributed to ineffective incident light collection, severe charge carriers' recombination, as well as sluggish reaction kinetics. The incorporation of GaN NWs would reduce the strong reflection of the planar silicon substrate (Boettcher et al., 2011) and facilitate the electron extraction (Zhou et al., 2019), thus improving the activity to some extent. However, owing to the lack of catalytic centers, GaN NWs/n^+-p Si still suffered from limited activity. The nanosheet-like Fe/n^+-p Si showed a similar *J-V* curve as GaN NWs/n^+-p Si, indicating the limited activity of nanosheet-like Fe at hundred-nanometers level. Surprisingly, Fe_{FAL}:GaN NWs/n^+-p Si at 80 cycles of iron electrodeposition shows a superior PEC behavior compared with that of both Fe/n^+-p Si and GaN NWs/n^+-p Si. The onset potential is +0.35 V versus RHE, with a prominent current density of −15.6 mA cm^{-2} at 0 V versus RHE. It is worth noting that a nearly saturated and high current density of ∼ −30 mA cm^{-2} is achieved at a minor overpotential of ∼0.2 V, which is approaching to the current density limit of silicon-based photocathode under standard one-sun illumination. The highest applied bias photo-to-current efficiency (ABPE) of 0.9% is acquired at an underpotential of 0.11 V with current density of −8 mA cm^{-2} (Figure S10). The number of the electrodeposition cycles of Fe cocatalyst affected the *J-V* curve significantly. The increase in electrodeposition, from 20 to 40 cycles, would lead to a gradual improvement in the PEC performance, ascribing to the increasing catalytic centers. An optimal activity is achieved at 80 cycles. However, at a higher loading, Fe_{200}:GaN NWs/n^+-p Si exhibits an evidently reduced activity with more negative onset potential and lower saturated current density (Figure 3B), in line with our expectation. It is likely due to the low catalytic activity of thick iron-base layer (Figure S11) (Fei et al., 2015). Based on these findings, it is reasonable to conclude that the high HER activity mainly arise from the few-atomic-layers iron on the lateral surface of GaN NWs, which is consistent with the results of density functional theoretical calculation described below, whereas the activity of larger-size iron is very limited. By comparing with the recent state-of-the-art HER catalysts (Table S1), we discovered that the Pt-based catalyst illustrated a higher positive onset potential of +0.4 V in contrast to that of +0.35 V for Fe_{FAL}:GaN NWs/n^+-p Si with a relatively better fill factor due to the accelerated kinetics (Figure S12). Nevertheless, this result did not change the conclusion that few-atomic-layers iron could be used as a promising HER catalyst resulting from its much lower price than that of noble metals like Pt. Under dark, the current density of Fe_{FAL}:GaN NWs/n^+-p Si is negligible, revealing that solar light is the energy force of the reaction. Additionally, no hydrogen was detected without external circuit regardless of illumination, indicating that this is a photoelectrocatalytic process.

Under the optimized conditions, the productivity and Faradaic efficiency of Fe_{FAL}:GaN NWs/n^+-p Si for hydrogen evolution reaction were evaluated at 0 V versus RHE. Under standard one-sun irradiation for 3,000 s, a relatively stable current density of about −16 mA cm^{-2} is achieved for hydrogen evolution (Figure 3C). As shown in Figures S13 and S14, STEM and XPS characterization revealed that the morphology and chemical oxidation of the as-prepared Fe_{FAL}:GaN NWs did not vary notably after the stability testing, suggesting the relative stability of the photo/electrocatalysts. Gas chromatography measurement indicated that the gas evolved from the working electrode was hydrogen from water reduction. Based on the calculation, the hydrogen evolution rate is as high as 306 μmol cm^{-2} h^{-1} based on geometric surface of the photocathode with high Faradaic efficiency of 98% (Figure 3D). At the same time, the counter electrode of Pt wire produced oxygen stoichiometrically from water oxidation. At the same time, trace amount of carbon monoxide was produced with a tiny Faradaic efficiency of <1%, which might originate from the reduction of HCO_3^- in the electrolyte. GC and H-NMR analyses suggested that no other carbon-based liquid and gaseous products were detected. These results provided a direct evidence that a large proportion of the photoinduced electrons were consumed for converting protons to hydrogen with high efficiency.

Density Functional Theory Calculations

To theoretically elucidate the enhanced PEC activity over Fe_{FAL}:GaN NWs/n^+-p Si at the atomic scale, DFT calculations were first conducted to investigate the geometry and interaction between the atomic Fe layers and GaN (please see Computational Methods for more details). Based on the characterization results, a slab model containing three-layer (3L) atomic Fe on the N-terminated surface of wurtzite-GaN(10ī0) was established to study the surface and interface properties of Fe_{3L}:GaN(10ī0). Top views of the optimized geometry for each layer of atomic Fe in Fe_{3L}:GaN(10ī0) are presented in Figure 4A. It was discovered that the first layer of Fe atoms prefers to sit at the top of N atoms on GaN(10ī0) surface with a Fe−N bond length of 1.98 Å, followed by the second and third layers favoring the hollow and Ga top sites, respectively (the layer-by-layer atomic configurations and corresponding relative energy are summarized in Figure S15
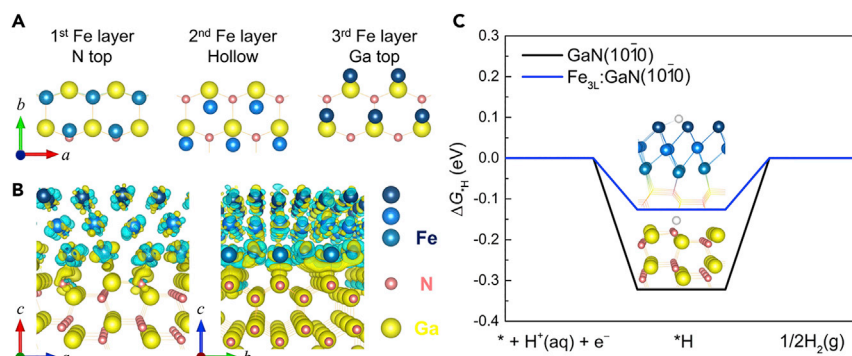
Figure 4. Density Functional Theory Calculations

(A) Top view of atomic geometries for the adsorbed first, second, and third Fe layers in the Fe_{3L}:GaN(10$\bar{1}$0) system along the c axis.

(B) Perspective views of the contour plots for the charge density redistribution near the interface region of Fe_{3L}:GaN(10$\bar{1}$0) along the b (left) and a (right) axis, respectively. Light yellow and light blue regions indicate the accumulation and depletion of electron density, respectively.

(C) Calculated free energy diagram of HER for pristine GaN(10$\bar{1}$0) and Fe_{3L}:GaN(10$\bar{1}$0) at zero applied potential.

Fe, blue; Ga, yellow; N, pink; H, white.

and Table S2). The Ga—N dimer formed from surface reconstruction on pristine GaN(10$\bar{1}$0) is flattened after the deposition of Fe atoms. Notably, the atomic geometry of Fe_{3L}:GaN(10$\bar{1}$0) optimized from DFT calculations is well matched with the STEM-HAADF characterization in Figure 2D, indicating the accuracy of our simulation model and method.

Besides, the electronic properties of Fe_{3L}:GaN(10$\bar{1}$0) were also investigated. As shown in Figure 4B, remarkable charge density redistribution is observed near the interface, suggesting a strong electronic coupling between Fe_{3L} and GaN(10$\bar{1}$0). Remarkable electron reduction (green color) occurs near the Fe atoms, whereas electron accumulation (yellow color) is observed around the neighboring N atoms, which is in good consistency with the XPS observation of a minor positive shift for Fe_{FAL}:GaN NWs/n$^+$-p Si compared with Fe/n$^+$-p Si (Figure S7). On the other hand, notable electron accumulation emerges around the middle region of the Fe and Ga atoms, which indicates the formation of covalent-like Fe—Ga bonds. These theoretical results regarding electronic properties reveal the formation of an efficient electron-transition channel that is highly favorable for the separation/migration of electron-hole pairs and for reducing the voltage loss during the reaction, which is in good agreement with the electrochemical measurement in the following.

It is noted that, in this study, Fe_{FAL}:GaN NWs/n$^+$-p Si was applied as a photocathode for water reduction toward hydrogen, whereas platinum wire was used as an anode for water oxidation toward oxygen. Therefore, the theoretical calculations were focused on the free energy of H adsorption on the catalysts surface of Fe_{FAL}:GaN NWs/n$^+$-p Si, i.e., G_{*H}, which is considered to be a key metric in quantitatively assessing the HER catalytic activity. Based on the computational hydrogen electrode (CHE) model suggested by Nørskov et al. (2004), a thermo-neutral value of ΔG_{*H} (i.e., 0 eV) at which the H adsorption is neither too strong or too weak on a catalyst surface is highly preferred for an ideal HER process. Employing DFT calculations, the free energy diagram of HER for both GaN(10$\bar{1}$0) and Fe_{3L}:GaN(10$\bar{1}$0) were mapped out, as illustrated in Figure 4C. As seen from the figure, ΔG_{*H} shows a value of −0.32 eV on the pristine GaN(10$\bar{1}$0) surface, indicating a rather strong binding of hydrogen with the N atoms on the surface. Such strong binding suggests that HER would be unfavorable to occur on a pristine GaN. On the other hand, the binding strength of H on the surface of the Fe_{3L}:GaN(10$\bar{1}$0) is significantly weakened, resulting in an optimal ΔG_{*H} value of −0.13 eV, comparable with that of a state-of-the-art HER catalyst of platinum (Nørskov et al., 2005). Additionally, to consider the possible oxidation that occurred on the surfaces, we conducted further theoretical calculation to study the effect of partially oxidized surface of Fe_{FAL}:GaN NWs/n$^+$-p Si on the H adsorption. We found that the ΔG_{*H} becomes even more thermo-neutral when the surface iron atoms are oxidized at different ratios (O coverages ranging from 8% to 33%), which indicates the formation of iron oxide would further enhance the superior performance of Fe_{FAL}:GaN NWs/n$^+$-p Si (Figures S16 and S17). Overall, the
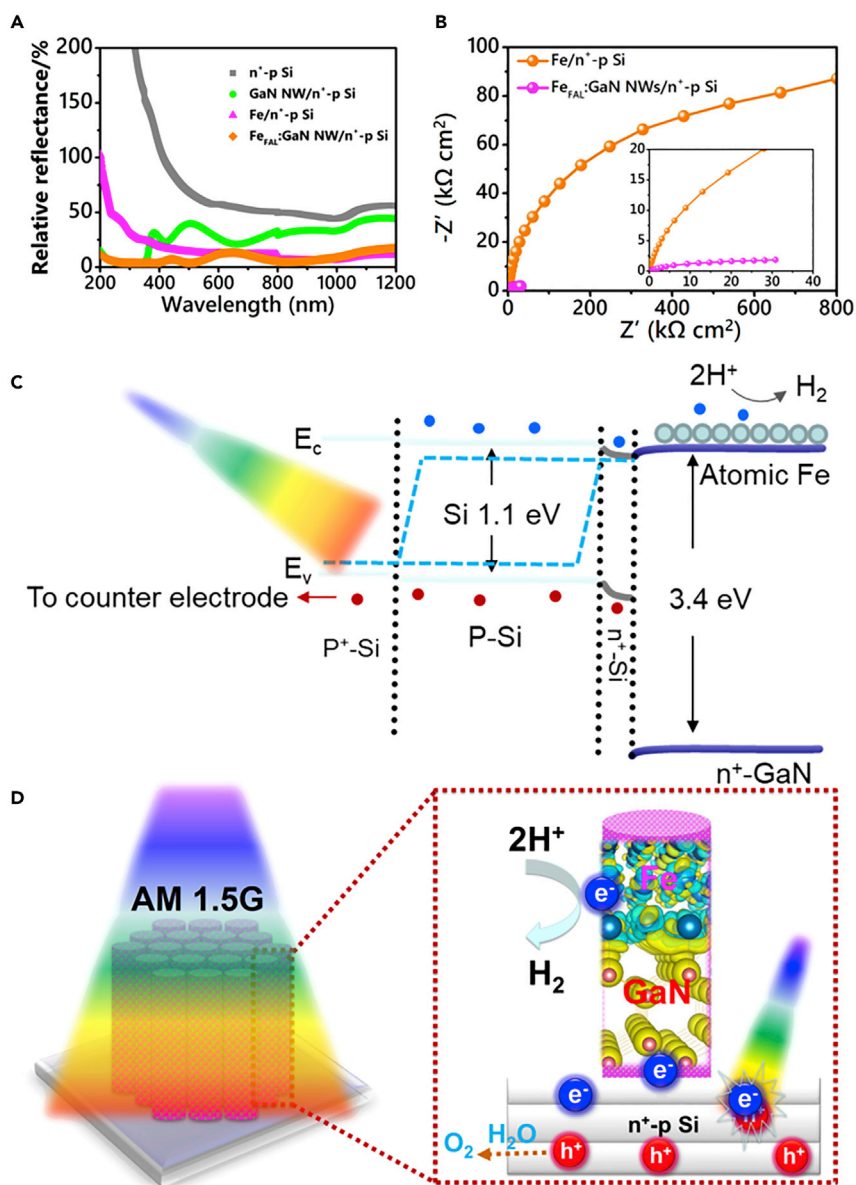
Figure 5. Proposed Mechanism

(A) UV-vis diffuse reflectance spectroscopy of n^+-p Si, Fe/n^+-p Si, GaN NWs/n^+-p Si, and Fe$_{FAL}$:GaN NWs/n^+-p Si.

(B) Electrochemical impedance spectroscopy of Fe/n^+-p Si and Fe$_{FAL}$:GaN NWs/n^+-p Si.

(C) The energy diagram of Fe$_{FAL}$:GaN NWs/n^+-p Si. Blue spot: electron, red spot: hole.

(D) Schematic illustration of Fe$_{FAL}$:GaN NWs/n^+-p Si for PEC water splitting toward hydrogen and oxygen under standard one-sun illumination.

superior HER performance of Fe$_{FAL}$:GaN NWs/n^+-p Si is attributed to the synergetic effect between the strong electronic coupling at the interface region and an optimal H adsorption strength.

To gain more insights into the superior performance, we carried out a series of optoelectronic measurements. Firstly, ultraviolet-visible (UV-vis) diffuse reflectance spectroscopy in Figure 5A illustrates that compared with planar silicon, GaN NWs/n^+-p Si demonstrates a remarkably improved light absorption due to the light-trapping effect. The integration of iron catalyst with GaN NWs further enhances the optical collection efficiency, rendering an excellent optical property for the reaction. Furthermore, the electronic property of Fe$_{FAL}$:GaN NWs/n^+-p Si photocathode was studied by electrochemical impedance

spectroscopy. The fitting equivalent circuit model of Fe_{FAL}:GaN NWs/n^+-p Si is shown in Figure S18. Electrochemical impedance spectroscopy in Figure 5B shows that the radius of Fe_{FAL}:Ga NWs/n^+-p Si is much smaller than that of Fe/n^+-p Si, suggesting that the electron resistance of Fe_{FAL}:GaN NWs/n^+-p Si is much lower than that of the nanosheet-like Fe/n^+-p Si (Ding et al., 2014). It reveals that the epitaxial GaN NWs can serve as an ideal electron-transition channel for charge carrier separation, which is verified by room temperature photoluminescence (PL) spectroscopy (Figure S19). Compared with GaN NWs/n^+-p Si, a dramatic reduction in PL intensity of Fe_{FAL}:GaN NWs/n^+-p Si suggests that the few-atomic-layers Fe reduces the radiative recombination of electrons and holes. It is well consistent with our previous observations (Zhou et al., 2020). The energy bandgap diagram of Fe_{FAL}:GaN NWs/n^+-p Si is shown in Figure 5C. Herein, the conduction band alignment between GaN and Si is almost negligible, as confirmed by our recent study (Vanka et al., 2018). Under illumination, the upward bending of surface is reduced by the accumulated photogenerated electrons. Hence, the photoinduced electrons can be easily extracted from n^+-Si to nearly dislocation-free n-GaN grown by highly controlled molecular beam epitaxy technology, which further migrate to atomic Fe layers with greatly reduced voltage loss. What is more, in such a unique nanoarchitecture, GaN nanowire is capable of maximizing catalytic centers. Together with the superior ΔG_{*H}, Fe_{FAL}:-GaN NWs/n^+-p Si is thus highly active for hydrogen production. Meanwhile, the holes migrate to the counter electrode via external circuit for oxygen evolution from water oxidation (Figure 5D).

Conclusion

In summary, Fe_{FAL} was anchored on GaN NWs/Si by a facile electrodeposition approach. Density functional theory calculations reveal an impressive hydrogen adsorption free energy of -0.13 eV on Fe_{FAL} as an indicator of high HER activity. Moreover, the strong electronic interaction between defect-free GaN and Fe_{FAL} provides an efficient electron-transition channel for charge carriers separation. Consequently, Fe_{FAL}:GaN NWs/n^+-P Si demonstrates a prominent current density of -15.6 mA cm^{-2} at 0 V with a decent onset potential of $+0.35$ V under standard one-sun illumination. The hydrogen evolution rate is as high as 306 μmol cm^{-2} h^{-1} with $\sim$98% Faradaic efficiency. The device, consisting of the two most produced semiconductors (Si and GaN) and earth-abundant material of iron as cocatalyst, is manufactured by mature epitaxial technology and electrodeposition. As such, this study presents a viable strategy for achieving economic, large-scale, and carbon-free hydrogen production from PEC water splitting using solar energy.

Limitations of the Study

This study has demonstrated that few-atomic-layers iron could be deposited on the N-rich m-plane surface of GaN NWs epitaxially grown on silicon substrate as an efficient photocathode for PEC water splitting toward hydrogen. However, the overall performance of the as-synthesized electrode is still relatively low compared with that of the state-of-the-art devices (Table S1). What is more, the morphology of the iron-based catalyst on the top surface of GaN NWs is difficult to be engineered to form atomic layers owing to the lack of spatial confinement, which is the most likely reason for the limited performance of the device. Further highly controlled synthesis of atomic-scale iron catalyst covered the entire GaN NWs will be conducted to improve the overall performance.

Resource Availability

Lead Contact
Further requests for resources and materials should be directed to and will be fulfilled by the Lead Contact, Zetian Mi (ztmi@umich.edu).

Materials Availability
This study did not yield new unique reagents.

Data and Code Availability
This study did not produce datasets/code.

METHODS

All methods can be found in the accompanying Transparent Methods supplemental file.

AUTHOR CONTRIBUTIONS

B.Z. and Z.M. conceived and designed the project. B.Z. and R.T.R. fabricated and characterized the samples and conducted the PEC testing. K.S. conducted the STEM characterizations. P.O. and J.S. performed DFT calculations and analyzed the calculation results. R.T.R. and S.V. carried out the nanowire arrays growth. L.Y. and H.S. contributed to result analysis and discussions. The manuscript was written by B.Z., P.O., J.S. and Z.M. with contributions from other co-authors.

DECLARATION OF INTERESTS

Some IP related to GaN nanowire synthesis was licensed to NS Nanotech, Inc., which was co-founded by Z.M.

REFERENCES

Arif, M., Yasin, G., Shakeel, M., Fang, X.Y., Gao, R., Ji, S.F., and Yan, D.P. (2018). Coupling of bifunctional CoMn-layered double hydroxide@graphitic C_3N_4 nanohybrids towards efficient photoelectrochemical overall water splitting. Chem. Asian J. 13, 1045–1052.

Boettcher, S.W., Warren, E.L., Putnam, M.C., Santori, E.A., Turner-Evans, D., Kelzenberg, M.D., Walter, M.G., McKone, J.R., Brunschwig, B.S., Atwater, H.A., and Lewis, N.S. (2011). Photoelectrochemical hydrogen evolution using Si microwire arrays. J. Am. Chem. Soc. 133, 1216–1219.

Camara, J.M., and Rauchfuss, T.B. (2012). Combining acid-base, redox and substrate binding functionalities to give a complete model for the [FeFe]-hydrogenase. Nat. Chem. 4, 26–30.

Cao, Y.J., Chen, S., Luo, Q.Q., Yan, H., Lin, Y., Liu, W., Cao, L.L., Lu, J.L., Yang, J.L., Yao, T., and Wei, S.Q. (2017). Atomic-level insight into optimizing the hydrogen evolution pathway over a Co_1-N_4 single-site photocatalyst. Angew. Chem. Int. Ed. 56, 12191–12196.

Chen, Y.J., Ji, S.F., Chen, C., Peng, Q., Wang, D.S., and Li, Y.D. (2018). Single-atom catalysts: synthetic strategies and electrochemical applications. Joule 2, 1242–1264.

Cheng, N.C., Stambula, S., Wang, D., Bains, M.N., Liu, J., Riese, A., Xiao, B.W., Li, R.Y., Sham, T.K., Liu, L.M., et al. (2016). Platinum single-atom and cluster catalysis of the hydrogen evolution reaction. Nat. Commun. 7, 13638.

Deng, J., Su, Y.D., Liu, D., Yang, P.D., Liu, B., and Liu, C. (2019). Nanowire photoelectrochemistry. Chem. Rev. 119, 9221–9259.

Ding, Q., Meng, F., English, C.R., Caban-Acevedo, M., Shearer, M.J., Liang, D., Daniel, A.S., Hamer, R.J., and Jin, S. (2014). Efficient photoelectrochemical hydrogen generation using heterostructures of Si and chemically exfoliated metallic MoS_2. J. Am. Chem. Soc. 136, 8504–8507.

Fan, L.L., Liu, P.F., Yan, X.C., Gu, L., Yang, Z.Z., Yang, H.G., Qiu, S.L., and Yao, X.D. (2016). Atomically isolated nickel species anchored on graphitized carbon for efficient hydrogen evolution electrocatalysis. Nat. Commun. 7, 10667.

Fei, H.L., Dong, J.C., Arellano-Jimenez, M.J., Ye, G.L., Kim, N.D., Samuel, E.L.G., Peng, Z.W., Zhu, Z., Qin, F., Bao, J.M., et al. (2015). Atomic cobalt on nitrogen-doped graphene for hydrogen generation. Nat. Commun. 6, 8668.

Feng, J.X., Wu, J.Q., Tong, Y.X., and Li, G.R. (2018). Efficient hydrogen evolution on Cu nanodots-decorated Ni_3S_2 nanotubes by optimizing atomic hydrogen adsorption and desorption. J. Am. Chem. Soc. 140, 610–617.

Gao, R., Zhang, H., and Yan, D.P. (2017). Iron diselenide nanoplatelets: stable and efficient water-electrolysis catalysts. Nano Energy 31, 90–95.

Le Goff, A., Artero, V., Jousselme, B., Dinh Tran, P., Guillet, N., Metaye, R., Fihri, A., Palacin, S., and Fontecave, M. (2009). From hydrogenases to noble metal-free catalytic nanomaterials for H_2 production and uptake. Science 326, 1384–1387.

Hashemi, S.M.H., Modestino, M.A., and Psaltis, D. (2015). A membrane-less electrolyzer for hydrogen production across the pH scale. Energ. Environ. Sci. 8, 2003–2009.

Hui, L., Xue, Y.R., Huang, B.L., Yu, H.D., Zhang, C., Zhang, D.Y., Jia, D.Z., Zhao, Y.J., Li, Y.J., Liu, H.B., and Li, Y.L. (2018). Overall water splitting by graphdiyne-exfoliated and -sandwiched layered double-hydroxide nanosheet arrays. Nat. Commun. 9, 5309.

Hui, L., Xue, Y.R., Yu, H.D., Liu, Y.X., Fang, Y., Xing, C.Y., Huang, B.L., and Li, Y.L. (2019). Highly efficient and selective generation of ammonia and hydrogen on a graphdiyne-based catalyst. J. Am. Chem. Soc. 141, 10677–10683.

Ji, L., McDaniel, M.D., Wang, S.J., Posadas, A.B., Li, X.H., Huang, H.Y., Lee, J.C., Demkov, A.A., Bard, A.J., Ekerdt, J.G., and Yu, E.T. (2015). A silicon-based photocathode for water reduction with an epitaxial SrTiO3 protection layer and a nanostructured catalyst. Nat. Nanotechnol. 10, 84–90.

Jin, J., Walczak, K., Singh, M.R., Karp, C., Lewis, N.S., and Xiang, C.X. (2014). An experimental and modeling/simulation-based evaluation of the efficiency and operational performance characteristics of an integrated, membrane-free,

neutral pH solar-driven water-splitting system. Energ. Environ. Sci. 7, 3371–3380.

Kibria, M.G., Qiao, R.M., Yang, W.L., Boukahil, I., Kong, X.H., Chowdhury, F.A., Trudeau, M.L., Ji, W., Guo, H., Himpsel, F.J., et al. (2016). Atomic-scale origin of long-term stability and high performance of p-GaN nanowire arrays for photocatalytic overall pure water splitting. Adv. Mater. 28, 8388–8397.

Kluwer, A.M., Kapre, R., Hartl, F., Lutz, M., Spek, A.L., Brouwer, A.M., van Leeuwen, P.W.N.M., and Reek, J.N.H. (2009). Self-assembled biomimetic [2Fe2S]-hydrogenase-based photocatalyst for molecular hydrogen evolution. Proc. Natl. Acad. Sci. U S A 106, 10460–10465.

Li, C.B., Li, Z.J., Yu, S., Wang, G.X., Wang, F., Meng, Q.Y., Chen, B., Feng, K., Tung, C.H., and Wu, L.Z. (2013). Interface-directed assembly of a simple precursor of [FeFe]-H₂ase mimics on CdSe QDs for photosynthetic hydrogen evolution in water. Energ. Environ. Sci. 6, 2597–2602.

Li, Q.H., Chen, W.X., Xiao, H., Gong, Y., Li, Z., Zheng, L.R., Zheng, X.S., Yan, W.S., Cheong, W.C., Shen, R.A., et al. (2018). Fe isolated single atoms on S, N codoped carbon by copolymer pyrolysis strategy for highly efficient oxygen reduction reaction. Adv. Mater. 30, 1800588.

Meng, C.H., Liu, Z.Y., Zhang, T.R., and Zhai, J. (2015). Layered MoS₂ nanoparticles on TiO₂ nanotubes by a photocatalytic strategy for use as high-performance electrocatalysts in hydrogen evolution reactions. Green Chem. 17, 2764–2768.

Nørskov, J.K., Rossmeisl, J., Logadottir, A., Lindqvist, L., Kitchin, J.R., Bligaard, T., and Jonsson, H. (2004). Origin of the overpotential for oxygen reduction at a fuel-cell cathode. J. Phys. Chem. B 108 (46), 17886–17892.

Nørskov, J.K., Bligaard, T., Logadottir, A., Kitchin, J.R., Chen, J.G., Pandelov, S., and Stimming, U. (2005). Trends in the exchange current for hydrogen evolution. J. Electrochem. Soc. 152, J23–J26.

Pullen, S., Fei, H.H., Orthaber, A., Cohen, S.M., and Ott, S. (2013). Enhanced photochemical hydrogen production by a molecular diiron catalyst incorporated into a metal-organic framework. J. Am. Chem. Soc. 135, 16997–17003.

Shi, L., Li, P., Zhou, W., Wang, T., Chang, K., Zhang, H.B., Kako, T., Liu, G.G., and Ye, J.H.

(2016). N-type boron phosphide as a highly stable, metal-free, visible-light-active photocatalyst for hydrogen evolution. Nano Energy 28, 158–163.

Tard, C., and Pickett, C.J. (2009). Structural and functional analogues of the active sites of the [Fe]-, [NiFe]-, and [FeFe]-hydrogenases. Chem. Rev. 109, 2245–2274.

Vanka, S., Arca, E., Cheng, S.B., Sun, K., Botton, G.A., Teeter, G., and Mi, Z.T. (2018). High efficiency Si photocathode protected by multifunctional GaN nanostructures. Nano Lett. 18, 6530–6537.

Vijselaar, W., Westerik, P., Veerbeek, J., Tiggelaar, R.M., Berenschot, E., Tas, N.R., Gardeniers, H., and Huskens, J. (2018). Spatial decoupling of light absorption and catalytic activity of Ni-Mo-loaded high-aspect-ratio silicon microwire photocathodes. Nat. Energy 3, 185–192.

Wang, F., Liang, W.J., Jian, J.X., Li, C.B., Chen, B., Tung, C.H., and Wu, L.Z. (2013). Exceptional poly(acrylic acid)-based artificial [FeFe]-hydrogenases for photocatalytic H2 production in water. Angew. Chem. Int. Ed. 52, 8134–8138.

Wang, A.Q., Li, J., and Zhang, T. (2018). Heterogeneous single-atom catalysis. Nat. Rev. Chem. 2, 65–81.

Wexler, R.B., Martirez, J.M.P., and Rappe, A.M. (2018). Chemical pressure-driven enhancement of the hydrogen evolving activity of Ni₂P from nonmetal surface doping interpreted via machine learning. J. Am. Chem. Soc. 140, 4678–4683.

Wodrich, M.D., and Hu, X.L. (2018). Natural inspirations for metal-ligand cooperative catalysis. Nat. Rev. Chem. 2, 0099.

Xue, Y.R., Huang, B.L., Yi, Y.P., Guo, Y., Zuo, Z.C., Li, Y.J., Jia, Z.Y., Liu, H.B., and Li, Y.L. (2018). Anchoring zero valence single atoms of nickel and iron on graphdiyne for hydrogen evolution. Nat. Commun. 9, 1460.

Ye, W., Fang, X.Y., Chen, X.B., and Yan, D.P. (2018). A three-dimensional nickel-chromium layered double hydroxide micro/nanosheet array as an efficient and stable bifunctional electrocatalyst for overall water splitting. Nanoscale 10, 19481–19491.

Yu, H.D., Xue, Y.R., Huang, B.L., Hui, L., Zhang, C., Fang, Y., Liu, Y.X., Zhao, Y.J., Li, Y.J., Liu, H.B., and Li, Y.L. (2019). Ultrathin nanosheet of graphdiyne-supported palladium atom catalyst for efficient hydrogen production. iScience 11, 31–41.

Zhang, H.X., Ding, Q., He, D.H., Liu, H., Liu, W., Li, Z.J., Yang, B., Zhang, X.W., Lei, L.C., and Jin, S. (2016). A p-Si/NiCoSeₓ core/shell nanopillar array photocathode for enhanced photoelectrochemical hydrogen production. Energ. Environ. Sci. 9, 3113–3119.

Zhang, M.L., Wang, Y.G., Chen, W.X., Dong, J.C., Zheng, L.R., Luo, J., Wan, J.W., Tian, S.B., Cheong, W.C., Wang, D.S., and Li, Y.D. (2017). Metal (Hydro)oxides@polymer core-shell strategy to metal single-atom materials. J. Am. Chem. Soc. 139, 10976–10979.

Zhang, H.B., An, P.F., Zhou, W., Guan, B.Y., Zhang, P., Dong, J.C., and Lou, X.W. (2018). Dynamic traction of lattice-confined platinum atoms into mesoporous carbon matrix for hydrogen evolution reaction. Sci. Adv. 4, eaao6657.

Zhao, Z.P., Liu, H.T., Gao, W.P., Xue, W., Liu, Z.Y., Huang, J., Pan, X.Q., and Huang, Y. (2018). Surface-engineering PtNi-O nanostructured with record-high performance for electrocatalytic hydrogen evolution reaction. J. Am. Chem. Soc. 140, 9046–9050.

Zhou, B.W., Kong, X.H., Vanka, S., Chu, S., Ghamari, P., Wang, Y.C., Pant, N., Shih, I., Guo, H., and Mi, Z.T. (2018). Gallium nitride nanowire as a linker of molybdenum sulfides and silicon for photoelectrocatalytic water splitting. Nat. Commun. 9, 3856.

Zhou, B.W., Kong, X.H., Vanka, S., Cheng, S.B., Pant, N., Chu, S., Ghamari, P., Wang, Y.C., Botton, G.A., Guo, H., and Mi, Z.T. (2019). A GaN:Sn nanoarchitecture integrated on a silicon platform for converting CO₂ to HCOOH by photoelectrocatalysis. Energ. Environ. Sci. 12, 2842–2848.

Zhou, B.W., Ou, P.F., Pant, N., Cheng, S.B., Vanka, S., Chu, S., Rashid, R.T., Botton, G., Song, J., and Mi, Z.T. (2020). Highly efficient binary copper-iron catalyst for photoelectrochemical carbon dioxide reduction toward methane. Proc. Natl. Acad. Sci. U S A 117, 1330–1338.

Supplemental Information

Few-Atomic-Layers Iron

for Hydrogen Evolution

from Water by Photoelectrocatalysis

Baowen Zhou, Pengfei Ou, Roksana Tonny Rashid, Srinivas Vanka, Kai Sun, Lin Yao, Haiding Sun, Jun Song, and Zetian Mi

Supplemental information

Transparent Methods

Procedure of few-atomic-layers iron deposited on GaN NWs. 2-inch silicon wafer (WRS Materials, 1-10 Ω·cm) was used for manufacturing n^+-p silicon junction through a standard thermal diffusion method. The wafer is first spin-coated with boron (Futurrex, Inc.) and phosphorous (Futurrex, Inc) as p- and n-type dopants, respectively; and then is applied to annealing at 950 °C under argon atmosphere in a furnace for 4 hours. Subsequently, the prepared junction is cleaned in buffered oxide etch solution. Prior to loading into the chamber for epitaxy growth, the silicon junction is further rinsed with acetone and methanol to eliminate contaminant. GaN NWs are epitaxially grown by a Veeco GEN II radio frequency plasma-assisted MBE system based on the well-established technology in our group. The growth is operated under nitrogen-rich atmosphere with a nitrogen flow rate of 1.0 cm^3 min^{-1}, and the temperature is kept at the range of 700-790 °C. The Ga beam equivalent pressure is 6×10^{-8} Torr. The forward plasma power is 350 W and the duration is 1.5 hours. Under this condition, GaN can be terminated with nitrogen atoms to provide sufficient nitrogen coordination sites, which has been widely confirmed by our previous studies (Kibria et al., 2016).

A series of Fe-based HER cocatalysts were electrodeposited on GaN NWs/n^+-p Si by a cyclic voltammetry (CV) method with different depositing cycles using Ag/AgCl as the reference electrode. Typically, GaN NWs/n^+-p Si was immersed in 1 mmol/L $FeCl_2$ aqueous solution (200 mL). Desired cycles of electrodeposition were first carried out from −0.5 to −2.0 V *vs.* Ag/AgCl at a scan rate of 100 mV/s. After that, the sample was applied to another CV scanning under the potential range from 0.1 to 2.0 V *vs.* Ag/AgCl at the same rate. The electrodeposited working electrode was then rinsed with distilled water and dried by dry

nitrogen thoroughly. Iron-based HER catalyst was electrochemically deposited on n^+-p silicon junction through the identical procedure for comparison. Similarly, Pt:GaN NWs/n^+-p Si was fabricated using H_2PtCl_6 aqueous solution (1 mmol/L) as the precursor by the same procedure for comparison.

Characterization of the electrodes. GaN NWs are scratched off the silicon wafer for STEM testing using a JEOL 2100 F microscope equipped with an aberration corrector at 200 kV. The SEM and EDS characterizations were carried out on an Inspect F-50 Facility for Electron (FE)-SEM system in McGill University. The oxidations states of each element of the photocathodes were characterized by a Kratos Axis Ultra XPS using a monochromatic Al source with energy solution ~0.5 eV. The optical property was conducted by a Cary 5000 UV-Vis-NIR spectrophotometer.

Photoelectrochemical reactions. The PEC testing was performed in a separated three-electrode-configuration chamber under argon atmosphere using 0.5 M $KHCO_3$ aqueous solution as the electrolyte. Prior to illumination, the electrolyte was purged with high-purity argon gas for at least 30 minutes. A solar simulator (Oriel LCS-100) was employed as the light source for the reaction. The intensity of the illumination approaching to the surface of the working electrode was calibrated to 100 mW cm^{-2} (AM 1.5G). Both Pt counter electrode and Ag/AgCl electrode were separated from the working electrodes by Nafion membranes to exclude the possibility that Pt was redeposited on the working electrode. The PEC testing and the electronic properties measurements were conducted on an Interface 1000E potentiostat (Gamry Instruments). The gas evolved from the working electrode and counter electrode were analyzed by gas chromatograph with a thermal conductivity detector (GC 8A, Shimadzu) and

a flame ionization detector (GC 2014, Shimadzu). H-NMR (Varian vnmrs 500) was applied to analyze the liquid reaction mixture in the presence of 1,3,5-trioxane as an internal standard.

DFT calculations. All spin-polarized calculations were based on the density functional theory (DFT) calculations (Kohn et al., 1965; Kresse et al., 1996) using the projector-augmented wave (PAW) method as implemented in the Vienna *ab initio* simulation package (VASP) code (Blöchl et al., 1994; Kresse et al., 1999). Electron exchange and correlation terms were described by BEEF-vdW functional (Wellendorff et al., 2012) that combines generalized gradient approximation with van der Waals correlation derived from the DFT-D2 method of Grimme (Grimme et al., 2006). The GaN NW was modeled by a 3×2 N-terminated surface of wurtzite-GaN($10\bar{1}0$), and the atomic geometries of Fe atoms in Fe_{3L}:GaN($10\bar{1}0$) were optimized by depositing them layer-by-layer. The energy cut-off for the plane-wave basis was chosen as 500 eV for all calculations, and structural optimization were achieved until the residual force of each ion was smaller than 0.01 eV $Å^{-1}$. The convergence criteria for the electronic structure was set to 10^{-5} eV per atom. All integrations over the Brillouin zone were performed using gamma-centered $2 \times 1 \times 1$ k-points. The electronic structure calculations employed a Fermi-level smearing width, taken as 0.05 eV for all adsorbed species, whereas 0.01 eV for all non-adsorbed species. A vacuum layer of more than 15 Å thickness was added along the vertical direction to avoid the artificial interaction between the periodic images.

Adsorbed and non-adsorbed species correction. The free energy diagram for HER was computed by adopting the computational hydrogen electrode (CHE) model proposed by Nørskov and co-workers (Nørskov et al., 2005). In the CHE model, the free energy for a pair of proton and electron $G(H^+ + e^-)$ in the solution can be directly treated by half of the free energy of hydrogen $0.5G(H_2)$. The free energy change (ΔG) for a reaction step is calculated as

$\Delta G = \Delta E + \Delta ZPE + \int \Delta C_p dT - T\Delta S$, where ΔE is the electronic energy difference directly obtained from DFT calculations, ΔZPE, $\int \Delta C_p dT$, and $T\Delta S$ are the changes in contributions from zero-point energies, heat capacities, and entropies, respectively. The temperature (T) is set to 298.15 K for a better comparison between current DFT calculation results with the experimental measurements.

The free-energies of adsorbed and non-adsorbed species were calculated by treating all of the $3N$ degrees of freedom as vibrational within the harmonic oscillator approximation, and then used to determine the zero-point energies, heat capacities, and entropies which are necessities to convert the electronic energies to free-energies.

Table S1. The summary of state-of-the-art photo/electrocatalysts for hydrogen evolution from water splitting. Related to Figure 3.

Photocathodes	Onset Potential (V *vs.* HRE)	Current density at 0 V *vs.* RHE (mA cm^{-2})	Refs.
Fe$_{FAL}$:GaN NWs/n$^+$-p Si	+0.35	-15.6	This work
MoS$_2$/p-Si	+0.25	-17.6	Ding et al., 2014
MoS$_x$@GaN NWs/n$^+$-p Si	+0.40	-40	Zhou et al., 2018
Pt/GaAsP/Si	+0.63	-4.5	Wu et al., 2014
Pt@SiO$_2$/pn$^+$-Si	+0.48	-30	Fan et al., 2016
Pt/2nm-Al$_2$O$_3$/pn$^+$-Si	+0.38	-25	Fan et al., 2014
WC$_2$/planar p-Si	+0.2	-5	Berglund et al., 2014
NiCoSe$_x$/planar p-Si	+0.07	-5.1	Zhang et al., 2016
CoP/planar n$^+$p Si	+0.46	-20	Hellstern et al., 2016

Table S2. DFT calculated relative energy of different atomic alignments for the first, second, and third layers of Fe atoms adsorbed on the GaN(10$\bar{1}$0) surface. The most stable adsorption site for each Fe layer are denoted in bold fonts. Related to Figure 4.

Number of Fe layers	Adsorption sites	Relative energy (eV)	Notes
1st Fe layer	Ga top	0.00106	Moved to N top
	Hollow	0	Moved to N top
	N top	0.00167	
2nd Fe layer	Ga top	0.49	
	Hollow	0	
3rd Fe layer	**Ga top**	0	
	N top	0.62	
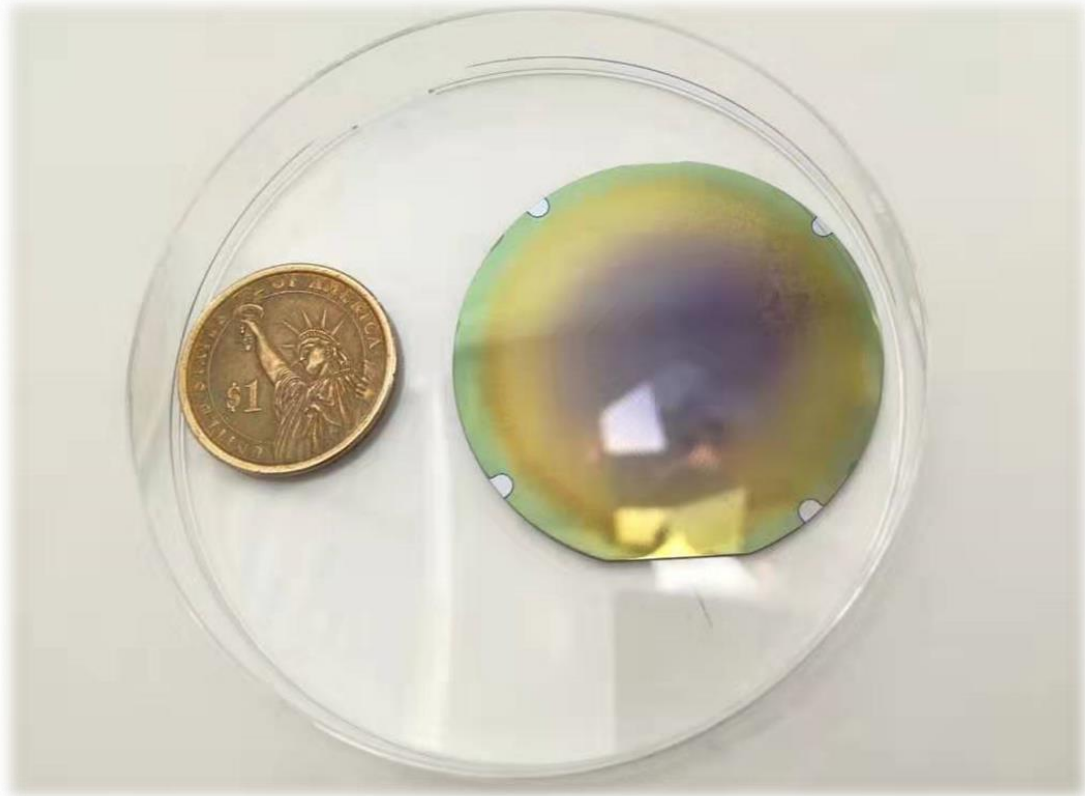
Figure S1. The photo of wafer-scale n^+-p Si junction decorated with GaN NWs. Related to Figure 1.
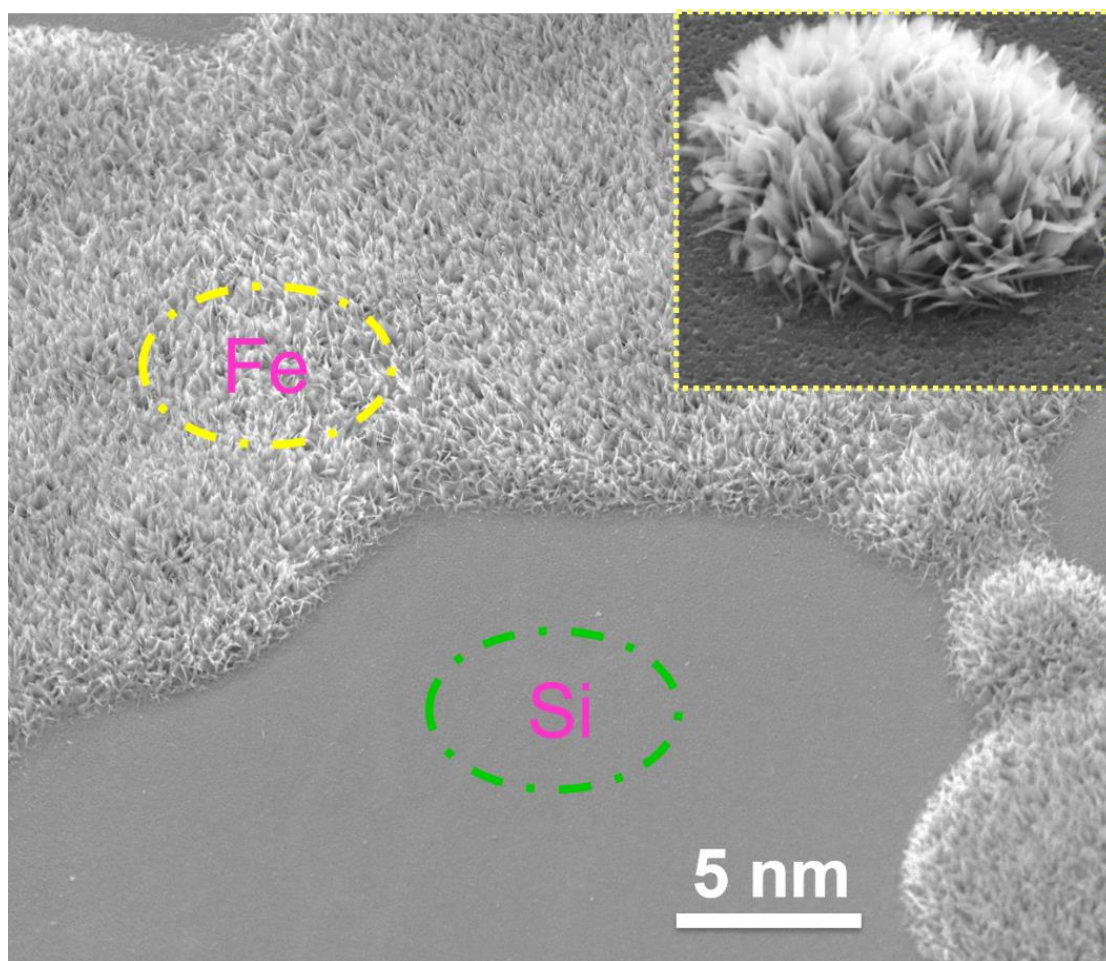
Figure S2. SEM images of Fe/n⁺-p Si. Inset is the SEM image for the iron catalyst on silicon substrate at high resolution. Related to Figure 2.
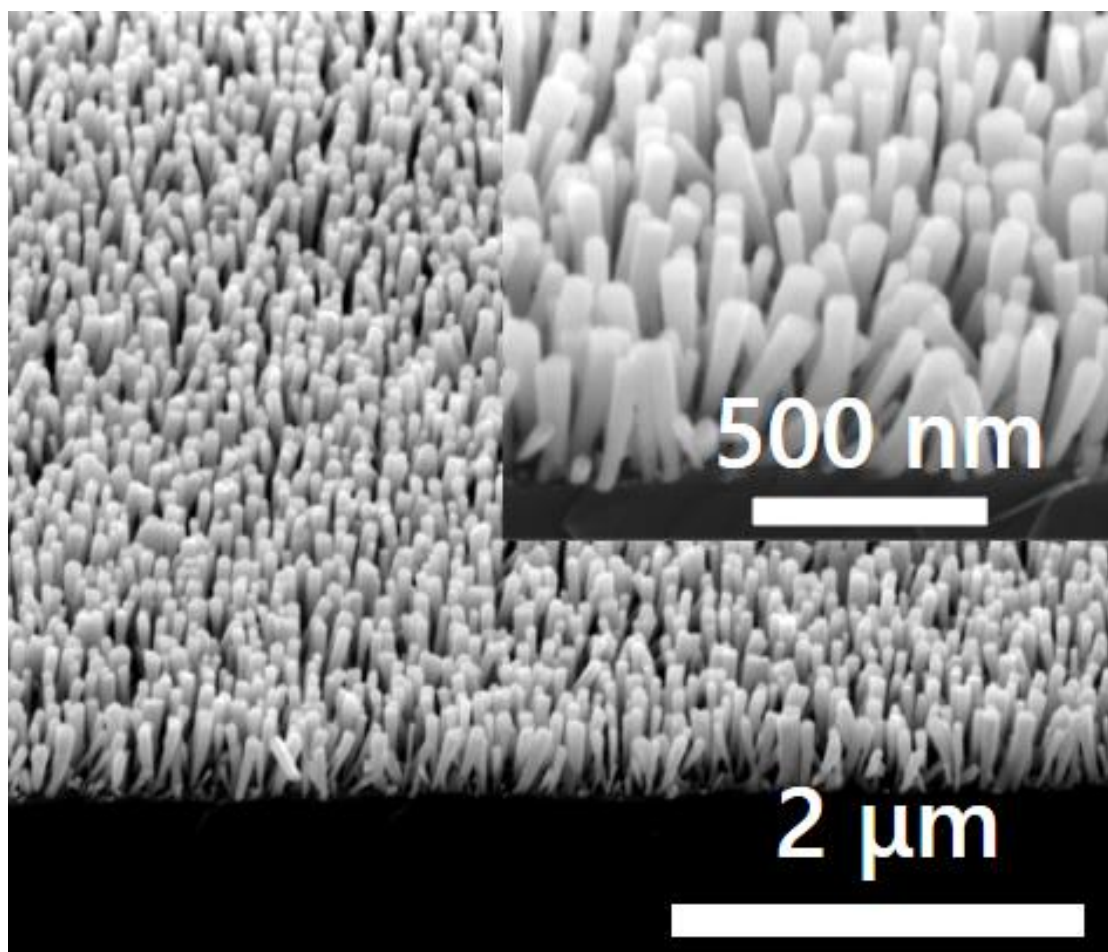
Figure S3. 45°-tilted SEM image of GaN NWs/n$^+$-p Si. Inset is the high-resolution SEM image. Related to Figure 2.
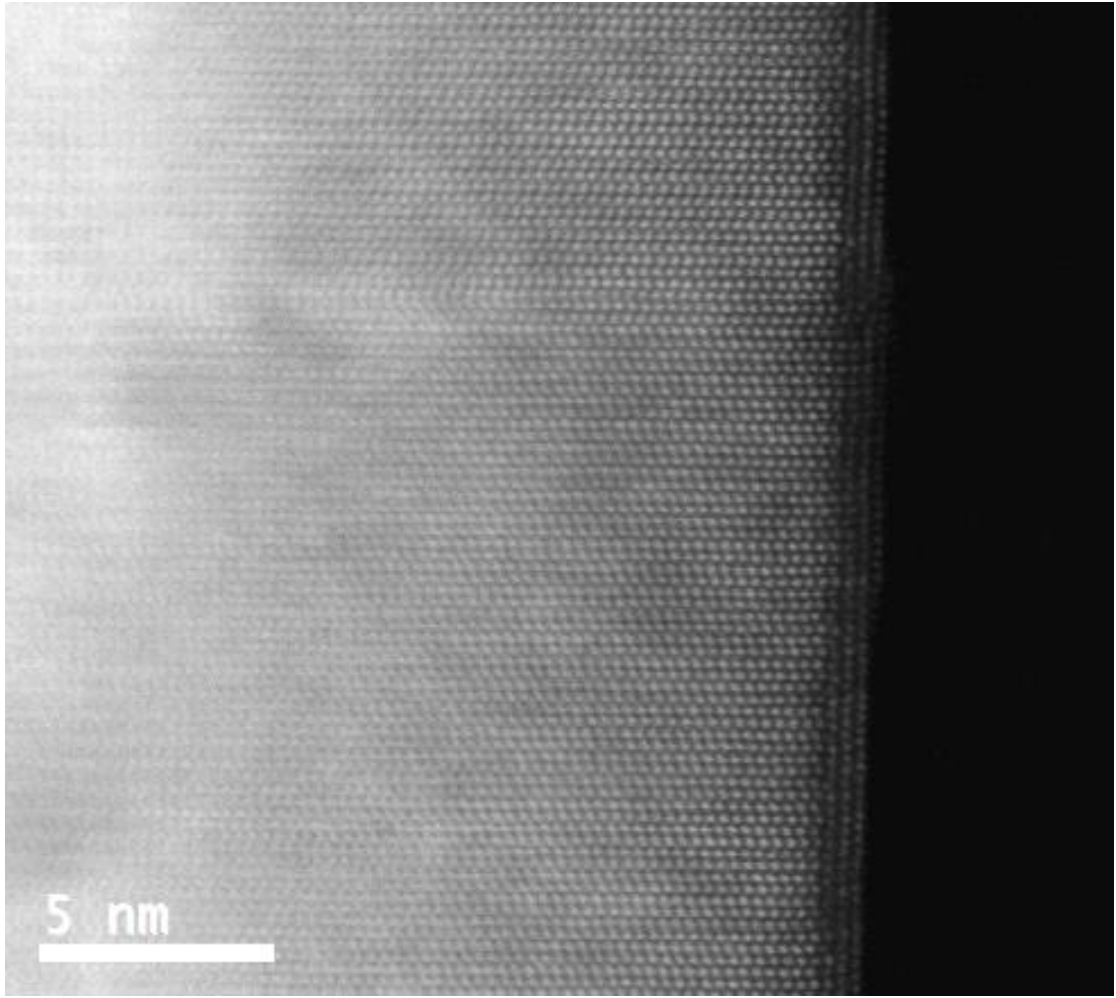
Figure S4. STEM-ADF image of Fe_{FAL}:GaN NWs/n^+-p Si. Related to Figure 2.
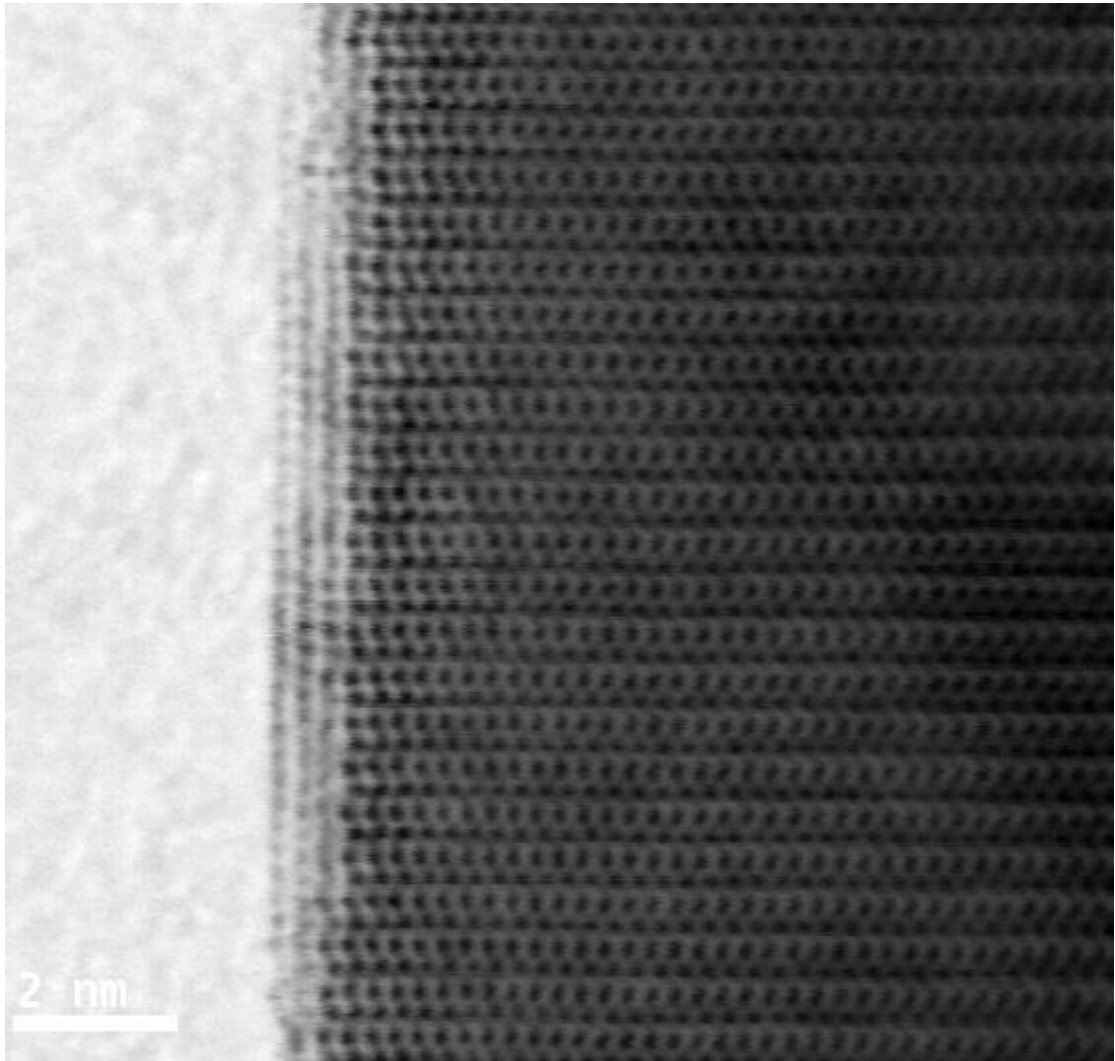
Figure S5. STEM-BF image of Fe_{FAL}:GaN NWs/n^+-p Si. Related to Figure 2.
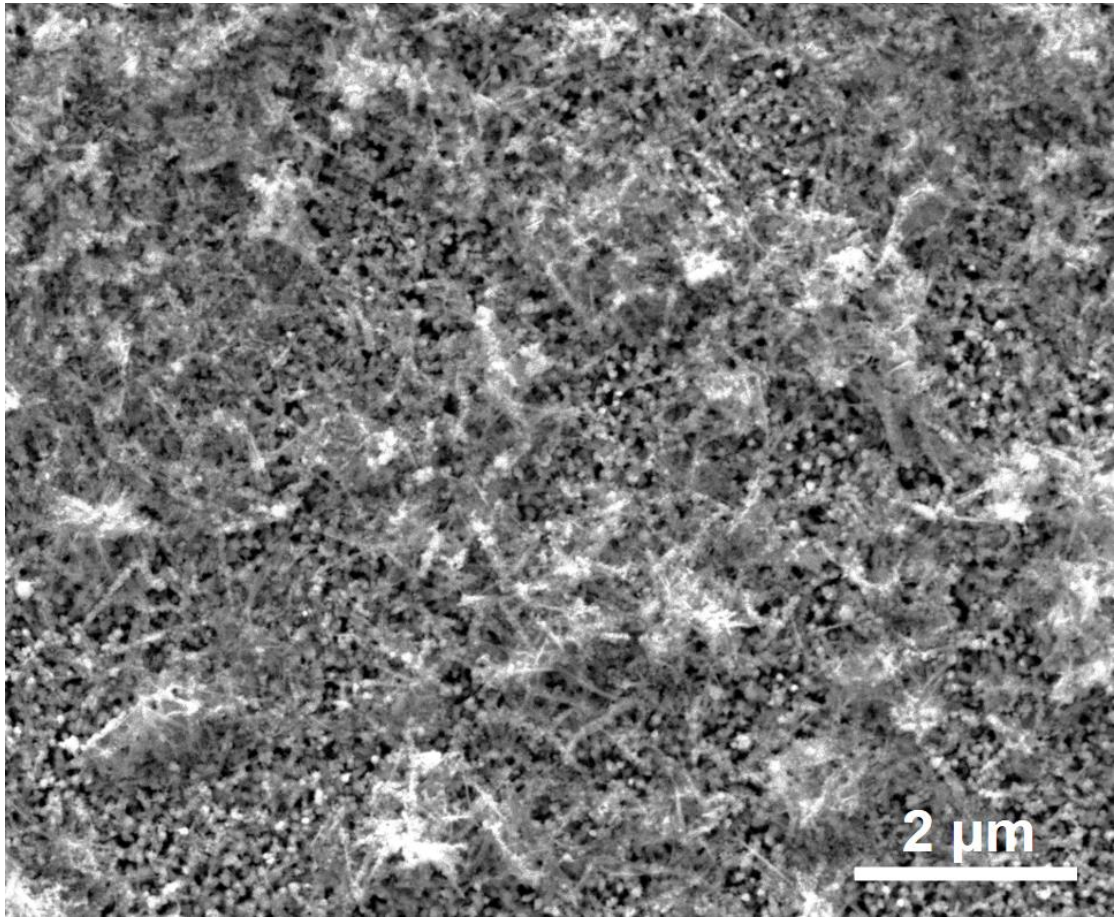
Figure S6. The top-view SEM image of Fe:GaN NWs/n$^+$-p Si at low resolution. Related to Figure 2.
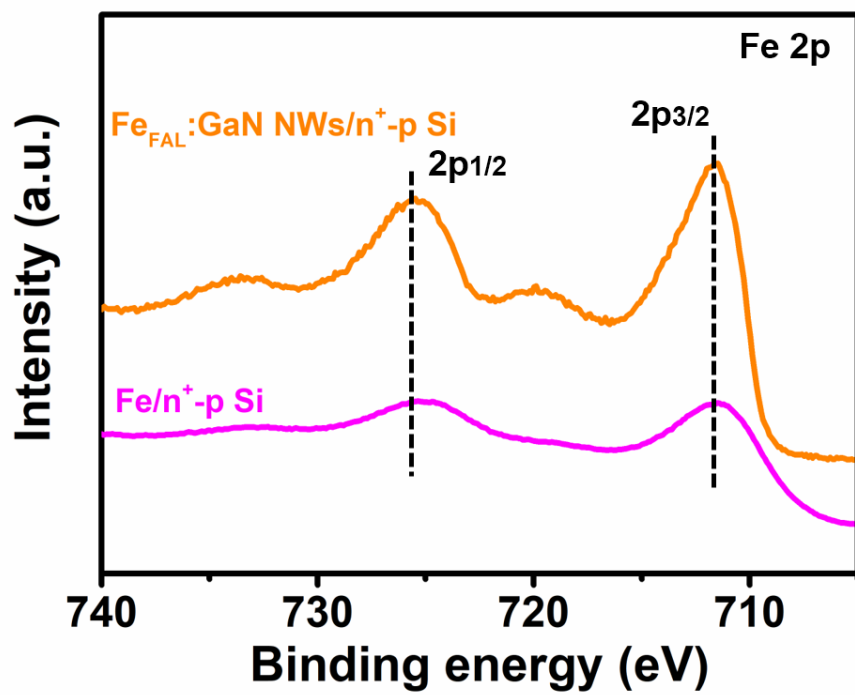
Figure S7. High-resolution XPS of Fe 2p of Fe/n$^+$-p Si and Fe$_{FAL}$:GaN NWs/n$^+$-p Si. Related to Figure 2.
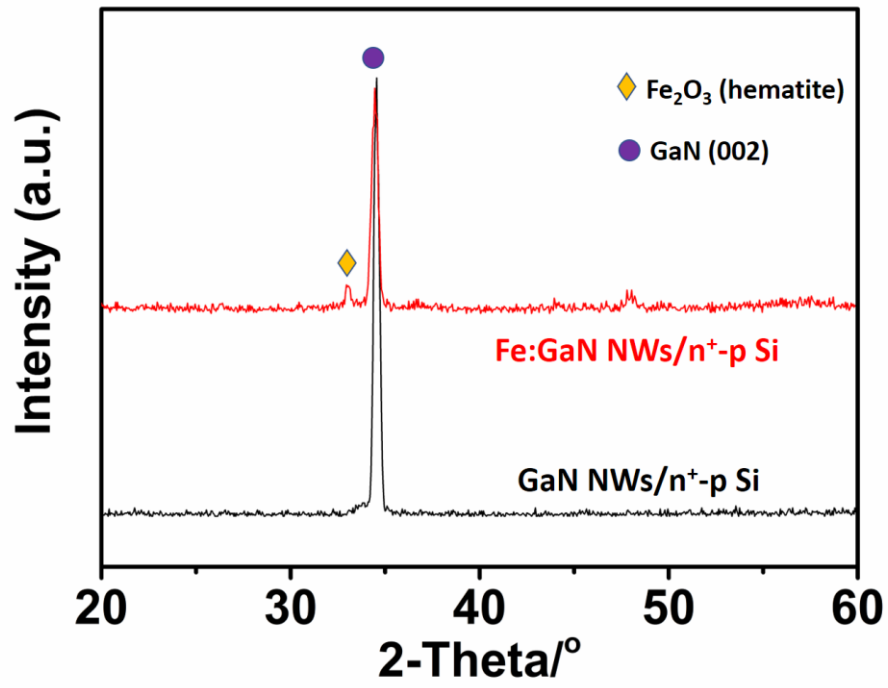
Figure S8. X-ray diffraction spectroscopy of GaN NWs/n^+-p Si and Fe:GaN NWs/n^+-p Si. Related to Figure 2.
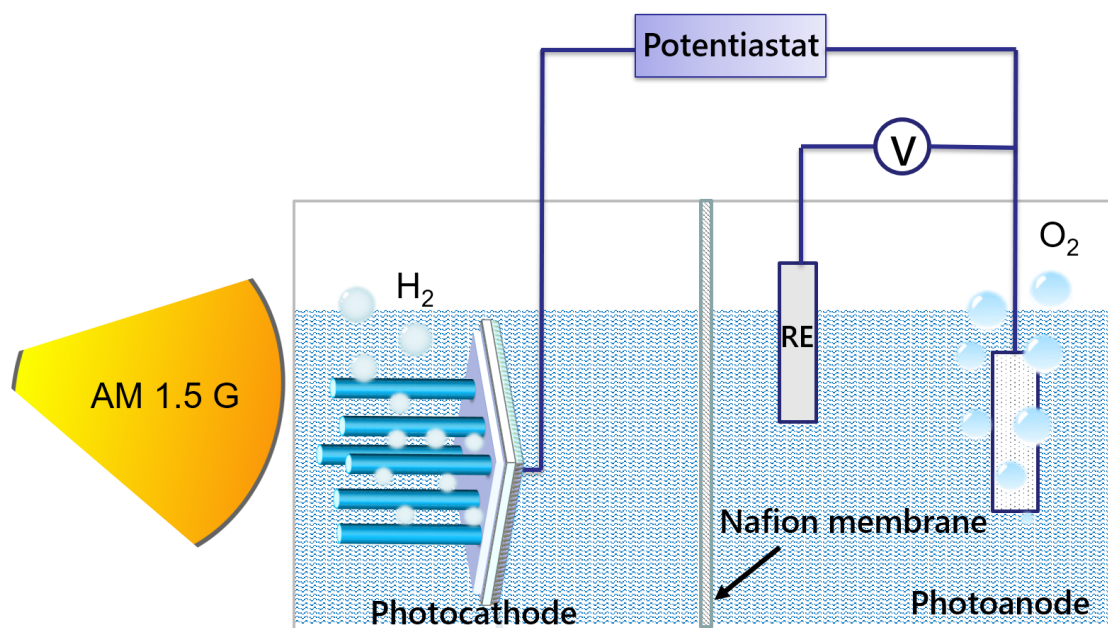
**Figure S9.** Schematic illustration of the three-electrode-configuration chamber for photoelectrocatalytic water splitting towards hydrogen. Related to Figure 3.
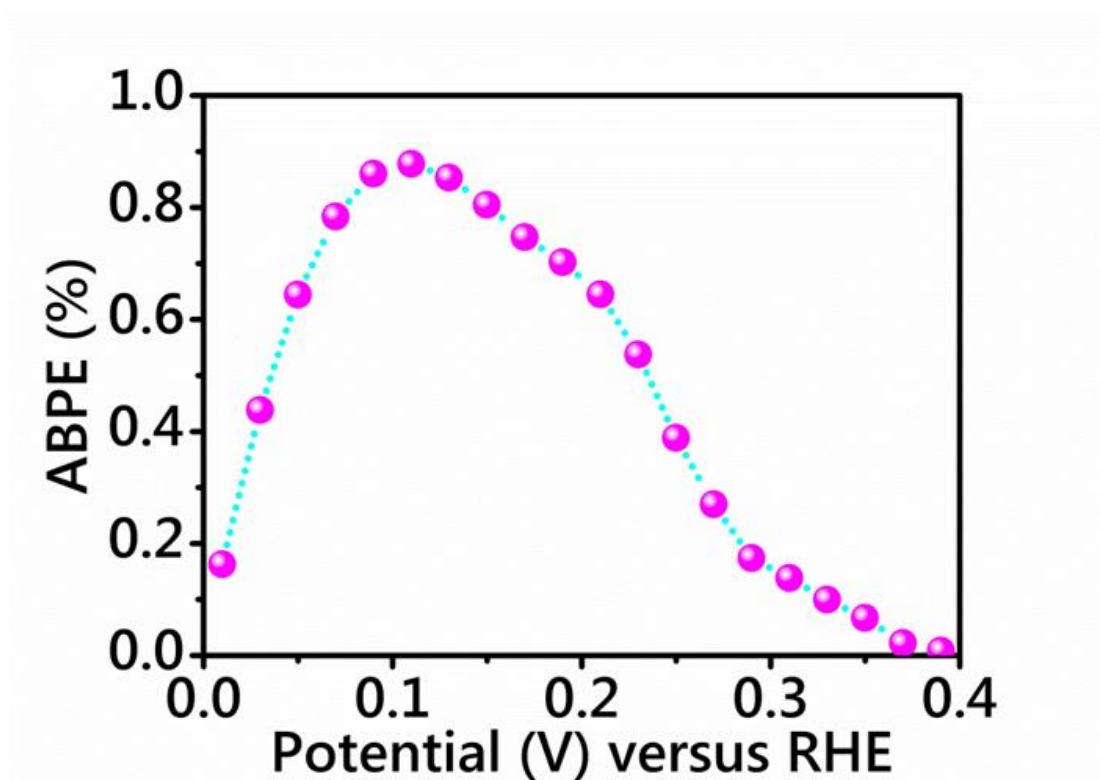
Figure S10. Applie bias photo-to-current efficiency (ABPE) of Fe_{FAL}:GaN NWs/n^+-p Si in argon-purged 0.5 M $KHCO_3$ aqueous solution under standard one-sun illumination. Related to Figure 3.
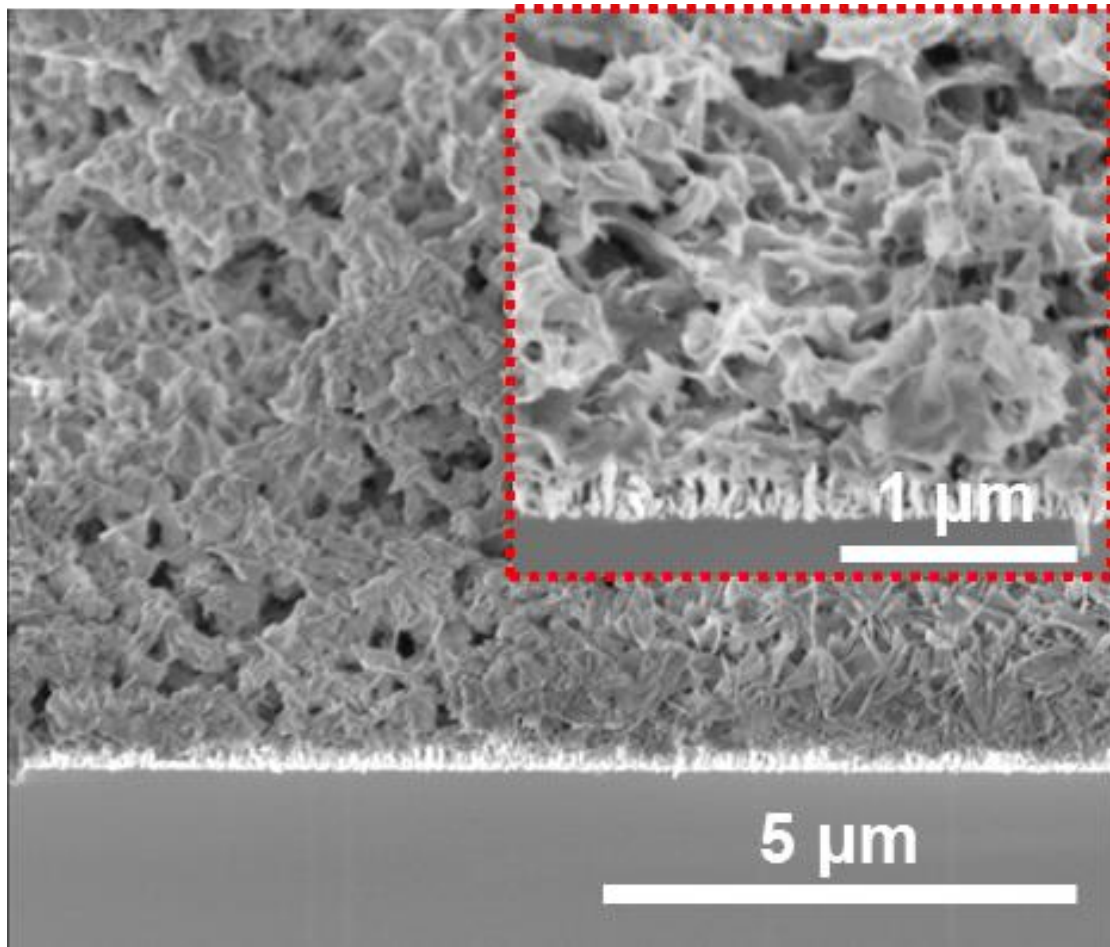
Figure S11. 45°-tilted SEM images of Fe$_{200}$:GaN NWs/Si with 200 cycles of electrodeposited Fe. Related to Figure 3.
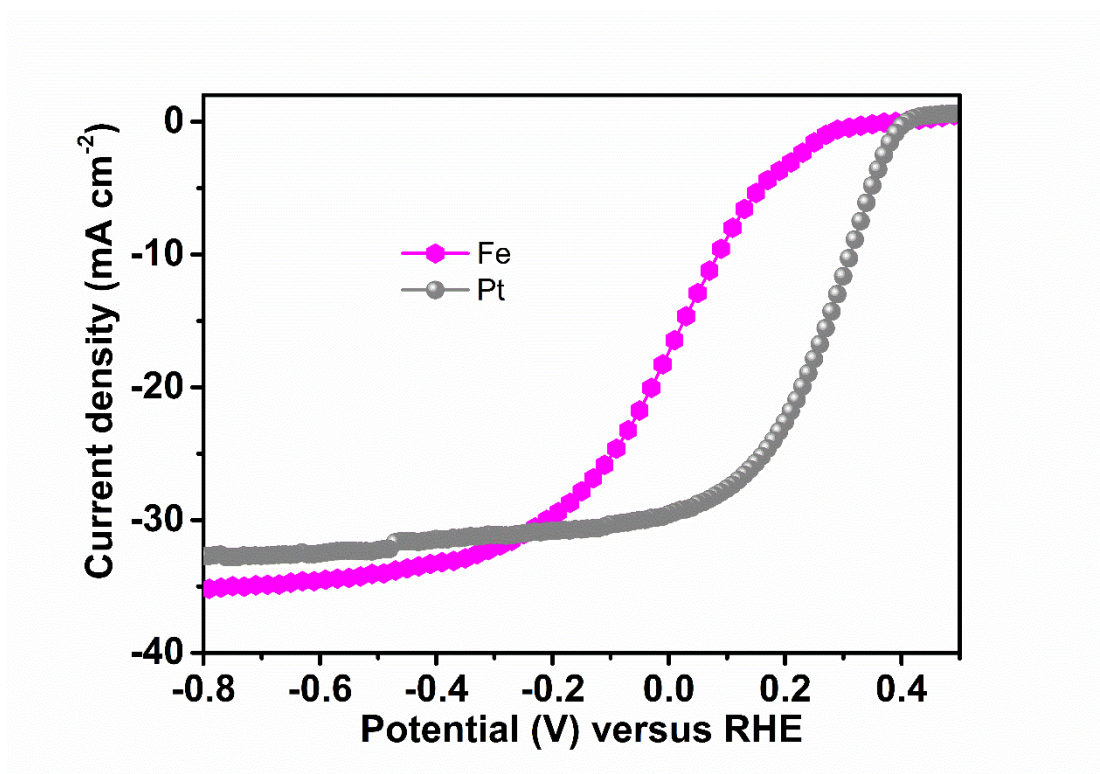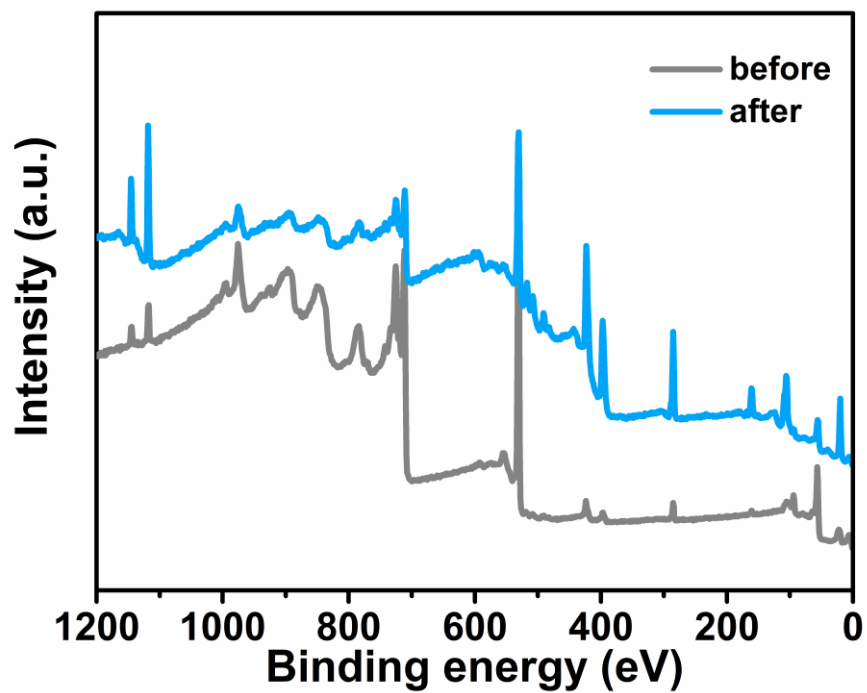
Figure S12. LSV curves of Fe_{FAL}:GaN NWs/n$^+$-p Si and Pt:GaN NWs/n$^+$-p Si under the identical experimental conditions. Experimental conditions: 0.5 M KHCO$_3$ aqueous solution, argon atomsphere, AM 1.5 G 100 mW cm^{-2}. Related to Figure 3.
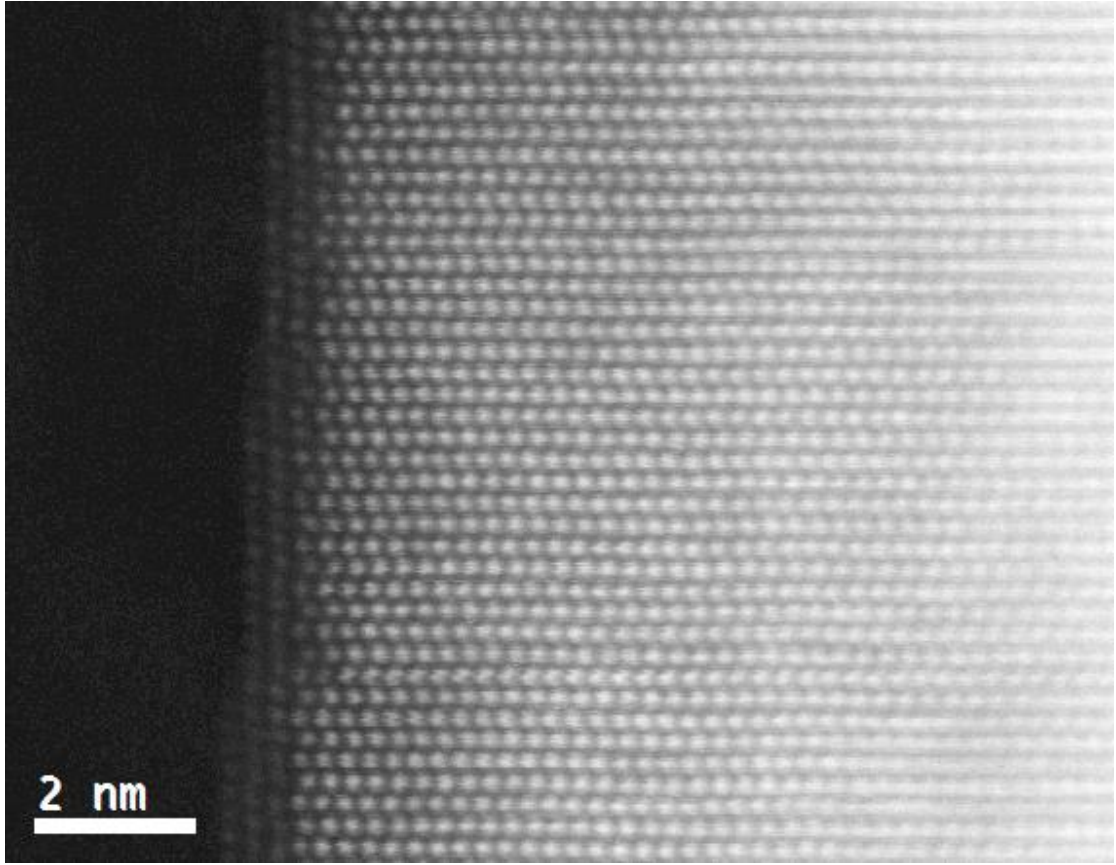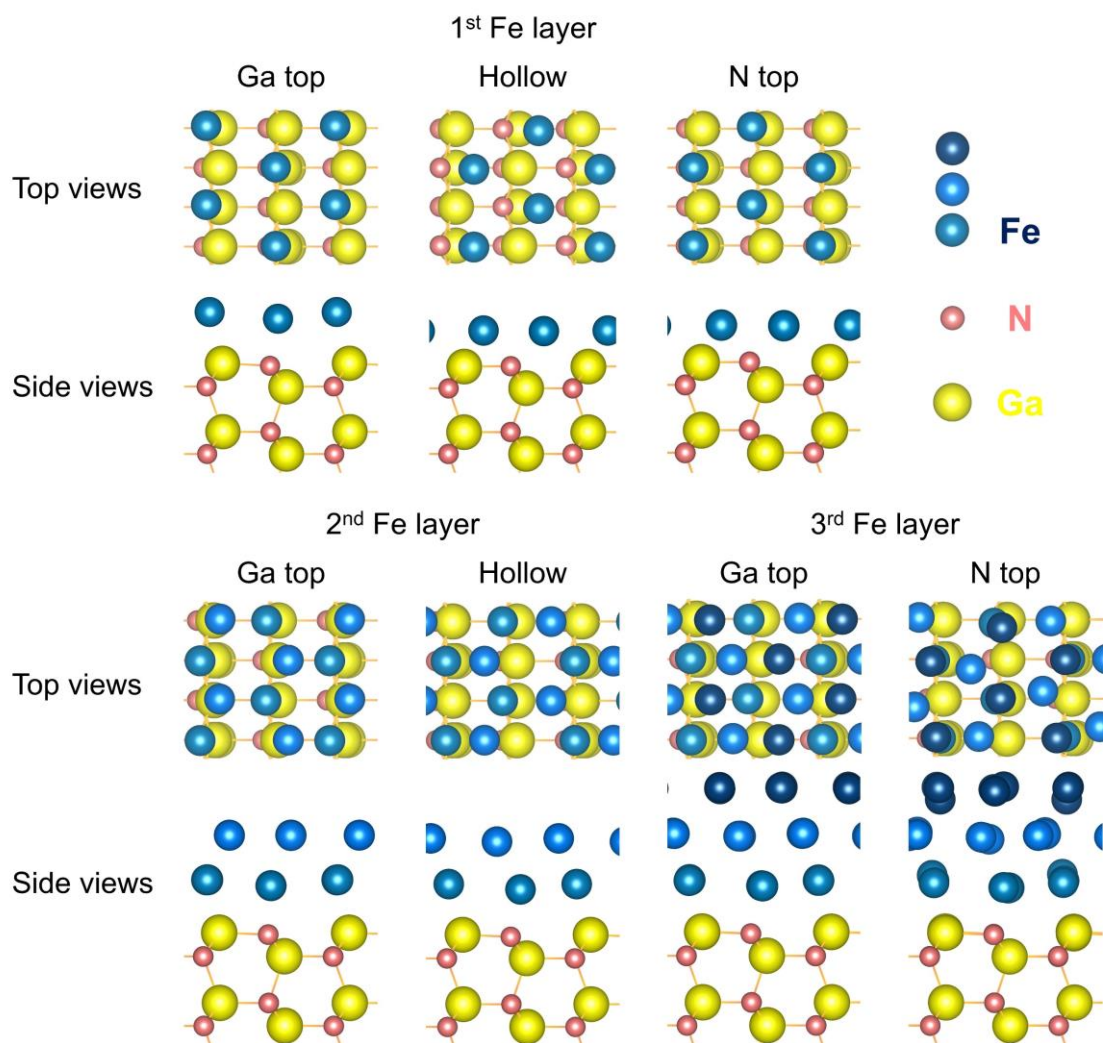
Figure S13. The STEM image of Fe$_{FAL}$:GaN NWs/n$^+$-p Si after stability testing. Related to Figure 3.

Figure S14. X-ray photoelectron spectroscopy measurement for Fe_{FAL}:GaN NWs/n^+-p Si before and after stability testing. Related to Figure 3.

Figure S15. Top and side views of the layer-by-layer atomic configurations for the first, second, and third layers of Fe atoms adsorbed on the GaN(10$\bar{1}$0) surface. Ga top, N top, and hollow represents for the adsorption site on the top of a Ga atom, N atom, and in a hollow consisted by 3 Ga and 3 N atoms, respectively. Fe, blue; Ga, yellow; N, pink; H, white. Related to Figure 4.
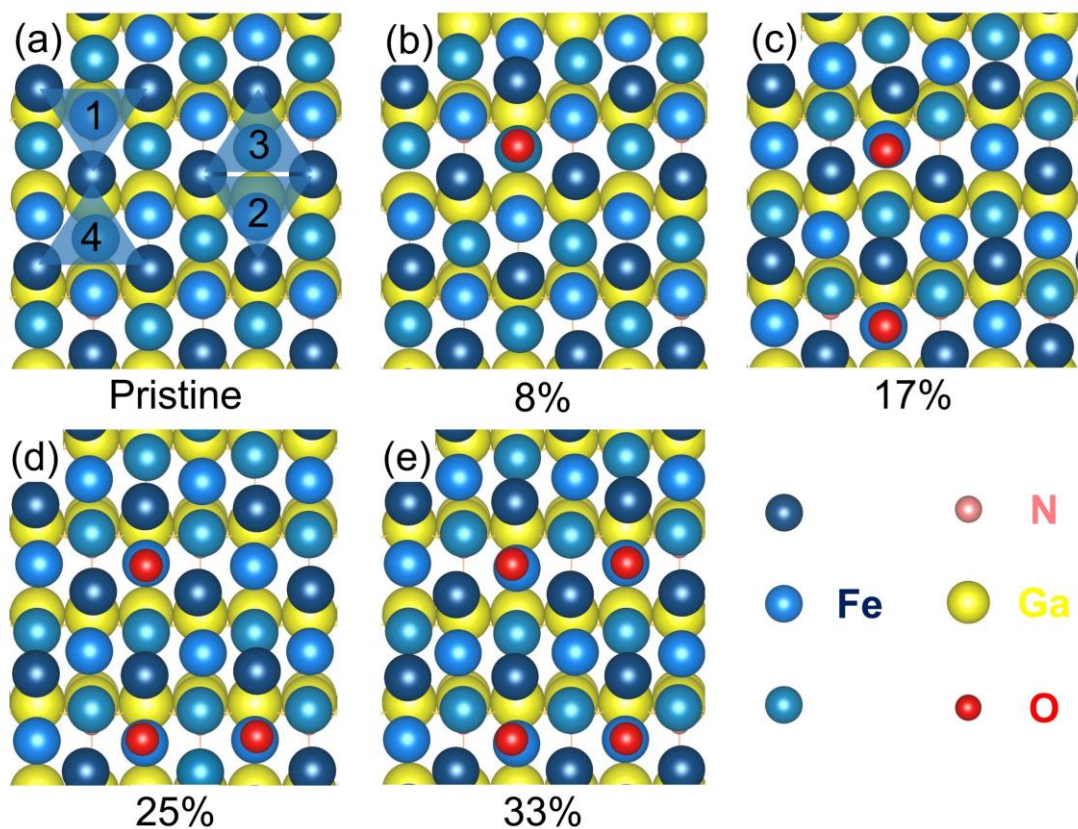
Figure S16. Optimized atomic configurations of pristine, and 8%, 17%, 25%, 33% coverages of oxygen atoms on the Fe surfaces in the Fe_{3L}:GaN($10\bar{1}0$). Fe, blue; Ga, yellow; O, red; N, pink; H, white. In subfigure (a), 4 different adsorption sites are shown, *i.e.*, fcc hollow sites (1, 2) and hcp hollow sites (3, 4) in (a), to obtain the averaged ΔG_{*H}. Related to Figure 4.
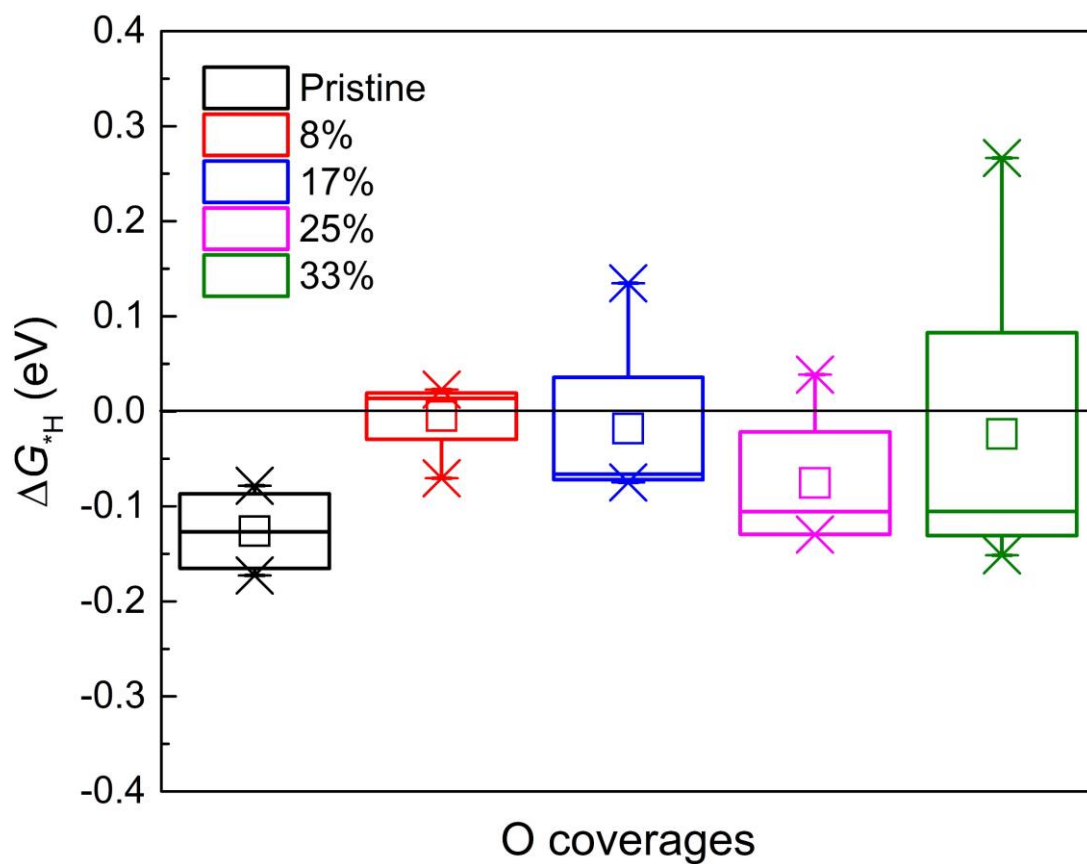
Figure S17. Boxplot of calculated G_{*H} on pristine and oxidized Fe_{3L}:GaN($10\bar{1}0$) surfaces at zero applied potential. The horizontal black line indicates the thermo-neutral value which is desirable for an ideal HER process. Related to Figure 4.
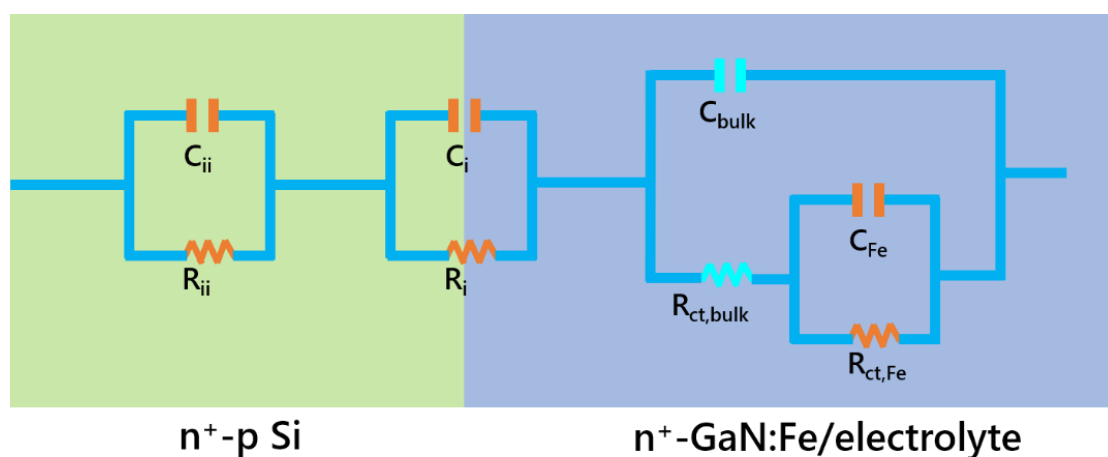
Figure S18. The fitting equivalent cuircuit for illustrating electronic properties of Fe_{FAL}:GaN NWs/n^+-p Si. R_i and C_i are band-bending with n^+-p silicon junction while R_{ii} and C_{ii} are for banding-bending between n^+-Si and n^+-GaN. C_{bulk} represents a constant phase element (CPE) for the bulk semiconductors of Si or GaN with the electrolyte while $R_{ct, bulk}$ signifies a charge transfer resisitance from semiconduction band. $R_{ct, Fe}$ is the charge resistance of Fe to the electrolyte; and C_{Fe} is CPE of Fe. Related to Figure 5.
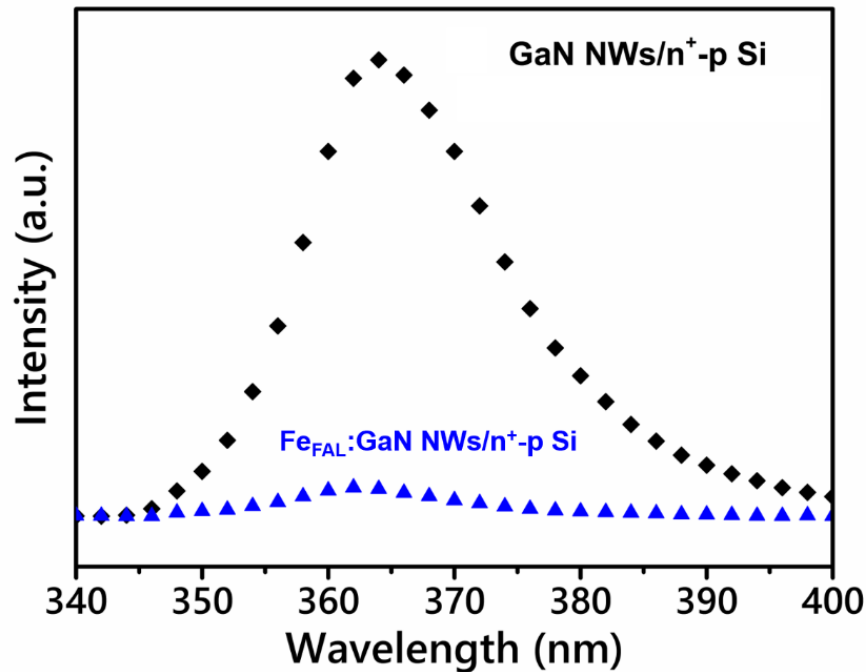
Figure S19. Room-temperature photoluminscence spectrum of GaN NWs/n$^+$-p Si and Fe$_{FAL}$:GaN NWs/n$^+$-p Si. Related to Figure 3. Related to Figure 5.

References

Kibria, M. G., Qiao, R. M., Yang, W. L., Boukahil, I., Kong, X. H., Chowdhury, F. A., Trudeau, M. L., Ji, W., Guo, H., Himpsel, F. J., Vayssieres, L. and Mi, Z. T. (2016). Atomic-scale origin of long-term stability and high performance of p-GaN nanowire arrays for photocatalytic overall pure water splitting. Adv. Mater. 28, 8388-8397.

Kohn, W. and Sham, L. J. (1965). Self-consistent equations including exchange and correlation effects. Phys. Rev. 140, A1133.

Kresse, G. and Furthmüller, J. (1996). Efficient iterative schemes for *ab initio* total-energy calculations using a plane-wave basis set. Phys. Rev. B 54, 11169-11186.

Blöchl, P. E. (1994). Projector augmented-wave method. Phys. Rev. B, 50, 17953.

Kresse, G. and Joubert, D. (1999). From ultrasoft pseudopotentials to the projector augmented-

wave method. Phys. Rev. B 59, 1758.

Wellendorff, J., Lundgaard, K. T. Møgelhøj, A., Petzold, V., Landis, D. D. and Nørskov, J. K. (2012). Density functionals for surface science: Exchange-correlation model development with Bayesian error estimation. Phys. Rev. B 85, 235149.

Grimme, S. (2006). Semiempirical GGA-type density functional constructed with a long-range dispersion correction. J. Comp. Chem. 27, 1787-1799.

Nørskov, J. K., Bligaard, T., Logadottir, A., Kitchin, J. R., Chen, J. G., Pandelov, S. and Stimming, U. (2005). Trends in the exchange current for hydrogen evolution. J. Electrochem. Soc. 152, J23-J26.

Ding, Q., Meng, F., English, C. R., Caban-Acevedo, M., Shear, M. J., Liang, D., Daniel, A. S., Hamers, R. J. and Jin, S. (2014). Efficient photoelectrochemical hydrogen generation using heterostructures of Si and chemically exfoliated metallic MoS_2. J. Am. Chem. Soc. 136, 8504-8507.

Zhou, B. W., Kong, X. H., Vanka, S., Chu, S., Ghamari, P., Wang, Y. C., Pant, N., Shih, I., Guo, H. and Mi, Z. T. (2018). Gallium nitride nanowire as a linker of molybdenum sulfides and silicon for photoelectrocatalytic water splitting. Nat. Commun. 9, 3856.

Wu, J., Li, Y. B., Kubota, J., Domen, K., Aagesen, M., Ward, T., Sanchez, A., Beanland, R., Zhang, Y. Y., Tang, M. C. Hatch, S., Seeds, A. and Liu, H. Y. (2014). Wafer-scale fabrication of self-catalyzed 1.7. eV GaAsP core-shell nanowire photocathode on silicon substrates. Nano Lett. 14, 2013-2018.

Fan, R. L., Tang, C. S., Xin, Y., Su, X. D., Wang, X. D. and Shen, M. R. (2016). Surface passivation and protection of Pt loaded multicrystalline pn^+ silicon photocathodes by atmospheric plasma oxidation for improved solar water splitting. Appl. Phys. Lett. 109, 233901.

Fan, R. L., Dong, W., Fang, L., Zheng, F. G., Su, X. D., Zou, S., Huang, J., Wang, X. S. and Shen, M. R. (2014). Stable and efficient multi-crystalline n+p silicon photocathode for H_2 production with pyramid-like surface nanostructure and thin Al_2O_3 protective layer. Appl. Phys. Lett. 106, 013902.

Berglund, S. P., He, H. C., Chemelewski, W. D., Celio, H., Dolocan, A. and Mullins, C. B.

(2014). p-Si/W$_2$C and p-Si/W$_2$C/Pt photocathodes for the hydrogen evolution reaction. J. Am. Chem. Soc. 136, 4, 1535-1544.

Zhang, H. X., Ding, Q., He, D. H., Liu, H., Liu, W., Li, Z. J., Yang, B., Zhang, X. W., Lei, L. C. and S. Jin. (2016). A p-Si/NiCoSe$_x$ core/shell nanopillar array photocathode for enhanced photoelectrochemical hydrogen production. Energy. Environ. Sci. 9. 3113-3119.

Hellstern, T. R., Benck, J. D., Kibsgaard, J., Hahn, C. and Jaramillo, T. F. (2016). Engineering cobalt phosphide (CoP) thin film catalysts for enhanced hydrogen evolution activity on silicon photocathodes. Adv. Energy Mater. 6, 1501758.